Examining controls on peak annual streamflow and floods in the Fraser River Basin of British Columbia

Charles L. Curry[1,2] and Francis W. Zwiers[1]

[1]Pacific Climate Impacts Consortium, University of Victoria, Victoria, V8N 5L3, Canada
[2]School of Earth and Ocean Sciences, University of Victoria, Victoria, V8N 5L3, Canada

Correspondence to: Charles L. Curry (cc@uvic.ca)

Abstract. The Fraser River basin (FRB) of British Columbia is one of the largest and most important watersheds in Western North America, and is home to a rich diversity of biological species and economic assets that depend implicitly upon its extensive riverine habitats. The hydrology of the FRB is dominated by snow accumulation and melt processes, leading to a prominent annual peak streamflow invariably occurring in June-July. However, while annual peak daily streamflow (APF) during the spring freshet in the FRB is historically well correlated with basin-averaged, April 1 snow water equivalent (SWE), there are numerous occurrences of anomalously large APF in below- or near-normal SWE years, some of which have resulted in damaging floods in the region. An imperfect understanding of which other climatic factors contribute to these anomalously large APFs hinders robust projections of their magnitude and frequency.

We employ the Variable Infiltration Capacity (VIC) process-based hydrological model driven by gridded observations to investigate the key controlling factors of anomalous APF events in the FRB and four of its subbasins that contribute more than 70% of the annual flow at Fraser-Hope. The relative influence of a set of predictors characterizing the interannual variability of rainfall, snowfall, snowpack (characterized by the annual maximum value, SWE_{max}), soil moisture and temperature on simulated APF at Hope (the main outlet of the FRB) and at the subbasin outlets is examined within a regression framework. The influence of large-scale climate modes of variability (the Pacific Decadal Oscillation (PDO) and the El Niño-Southern Oscillation (ENSO)) on APF magnitude is also assessed, and placed in context with these more localized controls. The results indicate that next to SWE_{max} (which strongly controls the annual maximum of soil moisture), the snowmelt rate, the ENSO and PDO indices, and rate of warming subsequent to the date of SWE_{max} are the most influential predictors of APF magnitude in the FRB and its subbasins. The identification of these controls on annual peak flows in the region may be of use in the context of seasonal prediction or future projected streamflow behavior.

1 Introduction

The Fraser River basin (FRB) of British Columbia (BC) is one of the largest watersheds draining the western slopes of the North American Cordillera, and home to both densely populated urban centres and a diversity of ecosystems closely linked

5 to the economic prosperity of the region (Fraser Basin Council, 2010). The FRB lies between the Coast Mountains and the Continental Divide, with the headwaters of the Fraser in the northeast (~53°N, 118°W) and its outlet at the Pacific Ocean in the southwest (Fig. 1). Its vast 240,000 km^2 area encompasses a range of climatic zones, from the snowy mountains of the eastern Rockies to dry interior plateaus, to wet fertile valleys nearest the Pacific west coast. The hydrological diversity of the basin is well described in Eaton and Moore (2010), who reviewed seasonal streamflow regimes at the catchment scale across

10 British Columbia, and also in Moore (1991), who focused specifically on the FRB. For the most part, streamflows are unregulated in the FRB, with the exception of Kenney Dam on the Nechako River in the northwest sector of the FRB (operational since the early 1950s) and several dams associated with the Bridge River power project in the Interior Plateau (completed in 1960). Regulated subbasins represent less than 10% of the total area of the FRB (Bawden, Burn and Prowse, 2015).

15   Streamflow in the interior catchments of the FRB is dominated by the snowmelt-fed spring freshet in June-July, leading to the usual characterization of the FRB as a nival basin. Hydrographs of major rivers in the FRB do not vary their form significantly from year to year due to the large amount of storage in the multi-year, high elevation snowpack. Indeed, the longest record of gauged flow at the southwestern outlet of the basin, at Fraser-Hope, has never recorded an annual peak daily flow (APF) outside of the April-July period (Water Survey of Canada hydrometric station 08MF005,

20 https://wateroffice.ec.gc.ca/search/historical_e.html). However, several catchments in the lower FRB, and to the west of the basin in the Coast Mountains and Western Cascades, exhibit a streamflow peak coinciding with the maximum of Pacific frontal rainstorm occurrence in October-December (Eaton and Moore, 2010).

1.1 Previous studies of climate and streamflow change in the FRB

25   The focus of this work is upon the main drivers of the interannual (and to some extent, interdecadal) variability in annual peak daily flow (hereafter APF), and not upon secular trends in APF in the FRB and its subbasins. However, as there is a growing body of work on such trends, which have implications for non-stationarity of the climate, we briefly review this research here, limiting the discussion to observations concerning APF magnitude. Significant long-term trends in temperature and precipitation have been detected over a network of meteorological stations in the FRB and its surroundings;

30 a summary of these trends is available in a recent report from the BC Ministry of the Environment (BC MOE, 2016) (in what follows, we average results for three regions used in the report which cover most of the FRB area: Sub-Boreal Interior,

Central Interior, and Southern Interior). Annual (summer ; winter) mean temperatures have increased at the rate of +0.9 °C century[-1] (+0.7 ; +1.4 °C century[-1]) over the 1900-2013 period, while minimum winter temperature has increased at the more rapid rate of 2.2 °C century[-1]. The latter coincided with reduced winter snow depth (−10% decade[-1]) and snow water equivalent (−6% decade[-1]; both over 1950-2014), mirroring a much larger-scale phenomenon occurring over Canada and the

5   U.S. (Gan et al., 2013; Knowles, 2015) and much of the Northern Hemisphere (Rupp et al., 2013; Jeong et al., 2017). On the other hand, precipitation amounts have increased in the FRB over 1900-2013, by about +2% decade[-1] in spring, summer, and fall, with no significant change in winter precipitation (BC MOE, 2016). However, sparse station coverage in the early decades of the twentieth century casts doubt on the robustness of this result. Restricting attention to the period 1950-2014, we used the regional data to compute precipitation trends of +3.3% decade[-1] in spring, +2.3% decade[-1] in fall and −4.1%

10 decade[-1] in winter, with no significant trend detected in summer. Over the last century (1912-2012), an earlier onset of the half-annual streamflow volume date was detected in one subbasin of the FRB (Stellako, 9-day advance) as well as at the major outlet to the basin at Hope (6-day advance). The latter conclusion was reinforced by Kang et al. (2016), who noted a statistically significant advance, by ~10 days, of the APF at Fraser-Hope over the 1949-2006 period.

        Recent decadal trends in the magnitude of annual and/or seasonal mean streamflow at gauge stations in BC and

15 western Canada have been investigated by several authors (Pike et al., 2010; Bawden et al., 2015; DeBeer et al., 2016; BC MOE, 2016), with no significant trends detected at stations in the FRB. Déry et al. (2012) and Hernández-Henríquez et al. (2017) conducted analyses on the FRB specifically, using a network of long-term measurements at 139 streamflow gauge stations available from the online Hydrometric Database (HYDAT; Water Survey of Canada, 2016). At Fraser-Hope specifically, Déry et al. (2012) found an increasing trend in interannual streamflow variability between 1960-2005, in both

20 annual and seasonal means, suggesting an increase in the frequency and/or intensity of low- and/or high-flow conditions, but with no detectable trend in annual mean streamflow at Hope.

        With respect to trends in the APF specifically, Cunderlik and Ouarda (2009) found no significant trend at most Reference Hydrometric Basin Network (RHBN) stations in the FRB over the 1974-2003 period, but noted a weak trend (~1-5%) toward decreasing magnitude and earlier APF occurrence at two stations. A Canada-wide nonstationary analysis by Tan

25 and Gan (2015), suggested that APF increased over recent decades at two stations in the FRB: the Stellako R. at Glenannan and Chilliwack R. at Chilliwack Lake. More aligned with our interests here, Burn and Hag Elnur (2002) found a weak negative correlation between APF and annual mean temperature at Quesnel in the FRB over the 1950-1997 period. We look for similar relationships between a range of climatic variables and APF at the scale of both the FRB and its major subbasins in Section 3 below.

30   Finally, it is important to recognize the influence of large-scale climate teleconnections on streamflow in the FRB. Previous researchers have investigated the influence of modes of large-scale climate variability on various river basins in western North America. Specifically, relationships between total and/or peak annual river discharge and the Pacific Decadal Oscillation (PDO), El Niño-Southern Oscillation (ENSO), and the Pacific North America index have been examined (Shabbar et al., 1997; Rood et al., 2005; Gobena and Gan, 2006; Bonsal and Shabbar, 2008; Whitfield et al., 2010; Gurrapu

et al., 2016). El Niño and La Niña typically occur every 3 to 5 years, often separated by 1 to 2 years of neutral conditions. The lower frequency PDO is a superposition of several interacting climate processes, including ENSO, mid-latitude ocean currents and atmospheric influences on mid-latitude sea surface temperatures (Alexander 2010). El Niño events are more likely to occur during the positive phase of the PDO, while La Niña events are more common during the negative phase.

5   During the negative (cold) phase of the PDO, and La Niña periods, winters in western Canada are typically cooler and wetter than average, with a larger snowpack at high elevations leading to higher annual discharge than average. Roughly opposite behaviour occurs during the positive (warm) PDO phase and occurrences of El Niño. Extending earlier work by Woo and Thorne (2003) and Thorne and Woo (2011), Gurrapu et al. (2016) determined that the PDO index is significantly anti-correlated ($p < 0.05$) with APF at 8 hydrometeorological stations in the FRB, while APF is correlated with the Southern

10 Oscillation Index (SOI), which tracks ENSO phase, at 11 stations. Specifically, both Thorne and Woo and Gurrapu et al. found that the observed APF was generally higher during the negative PDO phase and during La Niña years. For this reason, trends in climatic variables, including streamflow, are sensitive to the phase of the PDO and ENSO, which argues for a cautious interpretation of the results cited above.

15 **1.2 Characteristics of extraordinary historical floods in the FRB**

       While the FRB is primarily characterized as a nival basin, its large fractional area of lowlands with a relatively mild climate (e.g., mean December-January-February $T = 3.5$ °C at Hope) implies that the basin is sensitive to the precise seasonal development of warming temperatures and rainfall in spring. Both historical data and anecdotal accounts of large historical floods in the region place a large emphasis on the weather during the snowmelt period from early April to late June

20 as being a critical factor in the development of damaging floods (Septer, 2007). By one account, "the snow factor produces about 20-40% of the flood risk, while the weather factors produce about 60-80%" (BC River Forecast Centre, 2012). This fractional attribution is not supported by any quantitative assessment of the historical data, however, but rather can be considered an expert assessment (D. Campbell, private communication). Later in the paper, we present the results of a hydrological model simulation of the FRB driven by observed climate and spanning the period from 1955 to 2004. The

25 model framework permits an assessment of the separate roles of snowpack and weather factors by means of a multiple regression method and a qualitative analysis of high-magnitude floods in individual years. However, since the two largest known flood events in the FRB, in 1894 and 1948, occurred prior to this period, it is instructive to review the historical record of these events to form a preliminary impression of possible precursors.

30   A description of meteorological precursors to the 1894 and 1948 floods is available from the BC MOE (BC MOE, 2008) (see also the historical review, based on newspaper accounts, of Septer [2007]). According to the limited archival data available at two interior locations in the FRB, snowfall amounts during the winter of 1893-94 were near normal over the FRB as a whole, although the snowpack remaining from the previous summer was reportedly larger than usual (Septer,

2007). While the spring of 1894 was cold and wet in the FRB, temperatures rose rapidly in late May, becoming unseasonably warm near the end of that month. There is no reliable record of unusually large rainfall at this time. By the end of May, the Fraser overtopped its banks at many locations and existing dikes were breached, leading to the "Great Chilliwack Flood" in the densely populated Lower Fraser valley. The Fraser River at Mission (near Hope) peaked on June 5,

5   but floodwaters did not subside in many areas until early July. A hydrological modelling exercise conducted in 2008 estimated a peak discharge at Hope in the range of 16,000 to 18,000 m^3/s, with a best guess of 17,000 m^3/s (BC MOE, 2008).

The meteorological record for the FRB in 1948 is considerably more complete than for 1894. It shows that precipitation was well above normal for a long period in advance of the 1948 freshet, with excess rainfall in autumn 1947 and heavy snowfall in the subsequent winter and early spring. As a result, soils in many areas were likely near saturation at

10   the time of freeze-up, an important factor for the partitioning of runoff from spring snowmelt. Also, the accumulated reservoir of snow was larger than normal. The early spring of 1948 was cooler than average to May 20, followed by a rapid increase to unseasonably warm in late May-June. Thus, sensible heat inputs to the already high snowpack in the FRB were large, leading to a rapid and voluminous release of meltwater to lower elevations. Again, no excessive rainfall coincident with these events was recorded. The peak flow at Hope on May 31 was measured at 15,200 m^3/s, which remains the highest

15   value in the instrumental record to date (Septer, 2007; BC MOE, 2008).

The role of rainfall in historical flooding events in the FRB is likely restricted to smaller catchments and short time scales. Although there are numerous accounts of ill-timed rainfall augmenting already high water levels due to snowmelt on a section of the Fraser or one of its tributaries, these occurrences seem to be relatively rare and not the primary cause of overtopping. Rather, the historical record suggests that the main trigger of floods during the freshet is a rapidly melting

20   normal or larger than normal snowpack at upstream locations. During fall and winter, when peak rainfall occurs in the western FRB due to frontal storms making landfall from the Pacific, the potential exists for localized flooding—e.g., in urban areas due to runoff over impermeable surfaces—or for anomalous runoff due to rain-on-snow events. However, a different approach than the one we take here, which focuses on the maximum annual streamflow, would be necessary to investigate these types of events in the FRB.

25   The paper is structured as follows. Data sources, the VIC model and methods of analysis are described in Section 2. The main results of the study are gathered in Section 3, which begins with the regression analysis of observations before presenting insights from the VIC simulation results. Section 4 presents a few case studies that illuminate the precursors of high streamflow in particular years, and also reinforce the regression-based results. We conclude in Section 5 with a short discussion of outstanding issues and conclusions.

2 Data and Methods

2.1 Study domain and observational data

The domain of the study is the Fraser River Basin located in southwestern British Columbia (Fig. 1). Daily streamflow data were obtained from the WSC hydrometric database (HYDAT) for five hydrometric stations located within the FRB, as

5 summarized in Table 1. Manual snow survey (MSS) SWE measurements taken at the beginning of each non-summer month (8 times per year) were obtained from the British Columbia Snow Survey Network Program, distributed by the British Columbia River Forecast Center (http://bcrfc.env.gov.bc.ca/data/). The data do not permit the exact determination of the annual maximum SWE, so we extracted the April 1 SWE from each year for analysis. Data from 19 locations that are at least 81% complete spanning the period 1956-2014 were averaged to obtain an annual April 1 SWE time series for the entire

10 FRB. Exact locations of the MSS measurements are shown in Fig. 1 of Najafi et al. (2017).

We use the PDO and NINO3.4 indices to characterize the relevant large-scale climate modes affecting the region. The PDO index is derived as the leading principal component of monthly SST anomalies in the North Pacific Ocean northward of 20 °N (http://research.jisao.washington.edu/pdo/PDO.latest.txt). For the corresponding predictor variable, we use the mean PDO index from the preceding November to March, following Gurrapu et al. (2016). The NINO3.4 index is

15 calculated from the Hadley Centre sea surface temperature (SST) and sea ice gridded data set, HadISST1, as the area average of SST from 5 °S-5 °N and 170-120 °W, available from http://www.esrl.noaa.gov/psd/gcos_wgsp/Timeseries/Nino34/. We use the mean value from June to November of the preceding year as a predictor. Note that this differs slightly from Gurrapu et al., who instead made use of the SOI over the same months (NINO3.4 and the SOI are strongly negatively correlated).

The observational data set used for analysis and for driving the hydrological model (see below) is taken from the

20 gridded data set of surface temperature and precipitation at daily temporal and 1/16° spatial resolution described by Schnorbus et al. (2011), hereafter referred to as PCIC-OBS. The original station data, which span the period from January 1950 to December 2006, are interpolated to the grid and corrected for elevation using the Climate WNA package, which is based on PRISM (https://sites.ualberta.ca/~ahamann/data/climatewna.html; Hamann et al. 2013). Precipitation is not partitioned into rain and snow separately, but we estimate the snow-to-rain ratio as described in Section 3.2.3 below. A list of

25 all variables analyzed may be found in Table 2.

2.2 Hydrological model and boundary forcing

The gridded temperature and precipitation data described above were used to drive the variable infiltration capacity (VIC) hydrological model (Liang et al., 1994) over a large portion of British Columbia, including the FRB, from 1950-2006. The

30 VIC model is applied at a horizontal resolution of 1/16° (~5-6 km, depending on latitude), and solves the one-dimensional water and energy balance equations within each grid cell at a daily time step (with the exception of the snow sub-model, which runs at hourly resolution). Up to five elevation bands are used within each VIC grid cell, depending on the

topographic relief, by sampling a high-resolution digital elevation data set having 225 divisions within each 1/16° VIC cell. Each VIC grid cell can be assigned up to eight major vegetation classes, with a fractional cell area assigned to each, and these land cover fractions are identical for each elevation band within a VIC grid cell. Three of the input PCIC-OBS fields, maximum and minimum temperature and precipitation, are vertically interpolated to provide values for each elevation band

5   (the other input field, surface wind speed, is not interpolated). Surface and subsurface runoff are generated for each grid cell, and subsequently directed into a surface routing network (Lohmann et al., 1996, 1998; Schnorbus et al., 2011). Although VIC contains a parameterization for seasonally frozen soils (Cherkauer and Lettenmaier 1999), it was not implemented in the simulation we employed due to computational constraints. Simulated streamflow can be extracted at grid cells representing outlets of the FRB or any one of its subbasins, which can be evaluated against stream gauge measurements. VIC has been

10   calibrated and evaluated in the FRB and its subbasins (Schnorbus et al., 2010; Shrestha et al., 2012; Shrestha et al., 2014) and also in other nearby hydrological basins (Schnorbus et al., 2011). Recently, Islam and Déry (2017) used a lower horizontal resolution version of VIC (1/4°) to study its sensitivity to several different gridded input data sets, including PCIC-OBS. The authors found that while driving VIC with PCIC-OBS tended to overestimate SWE (see Sec. 3 below for a possible cause of this bias), the resultant hydrographs for the FRB and its basins were in better agreement with observations

15   than when competing data products were used as driving data sets. VIC model output variables, including SWE, total column soil moisture (both over the period 1950-2006), and routed streamflow at the location of WSC stations (1955-2004), were obtained from the Pacific Climate Impacts Consortium Data Portal (PCIC, 2016).

2.3 Selection of predictors and analysis methods

Predictors were selected based on physical intuition, inspection of the relevant literature and initial exploratory data
20   analysis. Prior studies that were particularly helpful in this regard were Gurrapu et al. (2016) who examined the influence of the PDO on streamflow in Western Canada, Jenicek et al. (2016) who examined the influence of snow accumulation and other variables on summer low flows, Coles et al. (2017) who studied snowmelt-runoff generation on Canadian prairie hillslopes, and Wever et al. (2017) who conducted model simulations of the joint effect of snowmelt and soil moisture on streamflow in a Swiss alpine catchment. The predictor variables chosen are listed in Table 2.

25   We explored relationships between interannual variations in the predictors and the predictand, the observed or VIC-simulated APF at Fraser-Hope. Both univariate and multivariate linear regression models were constructed for this purpose. The APF was determined as the maximum annual value of the running 3-day mean discharge at Fraser-Hope. Most of the predictors are represented as basin averages, but two, the ENSO and PDO indices, describe large-scale, multi-year climate modes of variability. The influence of large-scale climate can be manifested as nonstationary behaviour (e.g., trends) in the

30   predictand and/or predictors. Since regression models are sensitive to both trends and autocorrelation in the underlying time series, all univariate regressions were checked for the presence of both (e.g. ,see Shumway and Stoffer, 2010, and specifically their online supplement, https://onlinecourses.science.psu.edu/stat510/node/53).

Specifically, for the predictand (APF) Y_t and each predictor X_t, we first fit the models:

$$Y_t = \alpha_0 + \alpha_1 t + y_t , \qquad\qquad X_t = \beta_0 + \beta_1 t + x_t ,$$

where y_t and x_t are the corresponding detrended annual time series. If, as determined from the fit, there was no statistically significant temporal trend (with p-value < 0.05) in either Y_t or X_t, then Y_t and X_t themselves were used in the subsequent analysis in place of y_t and x_t. Trends were detected in certain of the time series analyzed in this work, as reviewed in Sec. 3.1

5 below. Regression models including variables with significant trends were generally found to have inflated correlation coefficients (e.g., Pearson's R^2 or Spearman's $\hat{\rho}$) compared to those using the same variables after detrending. The analysis proceeds using the fitted linear regression model to the detrended series y_t and x_t, i.e., $\tilde{y}_t = \gamma_0 + \gamma_1 x_t$. If a statistically significant relationship was found (again with p-value < 0.05), then the associated correlation coefficient is taken to be a conservative measure of the relationship between the predictand and predictor. We say "conservative" because it is possible

10 that the residuals $\varepsilon_t = y_t - \tilde{y}_t$ may yet possess an autoregressive structure, i.e. $\varepsilon_t = \phi_1 \varepsilon_{t-1} + \phi_2 \varepsilon_{t-2} + ... \phi_i \varepsilon_{t-i} + w_t$, where ϕ is the autocorrelation function (ACF) and w_t represents white noise (Shumway and Stoffer, 2010). If the sample ACF exceeds the standard threshold value of $2/\sqrt{N_{yr}}$ at any lag $i > 1$, where N_{yr} is the length of the time series, then further analysis would be required to fully specify the regression model. However, including autoregressive terms as predictors in the model will only increase the explained variance (e.g., Pearson's R^2), so we can be confident that the correlation coefficient after detrending,

15 but without including autoregressive terms, underestimates the correlation coefficient. In practice, however, autocorrelation was detected only in a few cases (using the function `acf2` in the R module `astsa`), and principally amongst predictors themselves, not in the regressions of APF on predictors.

Ultimately, the nonparametric Spearman's rank correlation, with sample estimator $\hat{\rho}$, was used to characterize the univariate regression results as it makes no assumptions regarding the distribution of the climatic and hydrologic data. A

20 correlation matrix of $\hat{\rho}$ was constructed by repeated univariate regression over all variables (including detrending where necessary), and the results summarized in the correlograms presented in Section 3.

Multilinear regression (MLR) analyses were also conducted by including all possible combinations of the predictors listed in Table 2. We retained the MLR model that featured: 1) the most variables (N) with partial p-values less than 0.05 (N_{sig}), and; 2) a Pearson-adjusted coefficient of determination R_{adj}^2 larger than any MLR with $N < N_{sig}$ predictors. We also

25 tried adding predictors in a stepwise manner, but obtained similar results.

3 Results

3.1 Trends in observed time series

We begin by searching for temporal trends in the input time series using linear least-squares regression. These are of interest on their own, but also for interpreting the results of the univariate and multivariate regression models later in this section. In

30 addition to APF, we computed linear fits for the eight observed variables listed in Table 2 over the common period of record 1956-2006, with the results summarized in Table 3. Of the nine variables, four display statistically significant trends at the $p < 0.05$ level: APF, freezing degree days (absolute value of the sum of negative daily mean $T < 0$ °C from October 1 – March

31, hereafter FDD), April-June mean temperature (T_{amj}), and the PDO index. The correlation coefficient R^2 is small for all the fits ($R^2 = 0.10-0.16$), indicating that the trends are modest compared to the scatter in the annual data. The decreasing trend in FDD and increasing trend in April-June mean temperature (0.26 °C decade^{-1}) are qualitatively consistent with the regional temperature trends summarized in Sec. 1.1. The trend in APF of −37 m^3 s^{-1} y^{-1}, or −4.3% decade^{-1} is of the same

5   sign but lower magnitude than that estimated for annual mean flow at Hope by BC MOE (2016) (−5.7% decade^{-1} between 1958-2012). However, it is worth noting that over the entire 1912−2014 period of the gauge record at Fraser-Hope, there is no significant trend detected in APF, even at the less conservative p-level of 0.1. The same is true of the PDO index over its much longer period of record (1900-2015). Nevertheless, we detrended the 1956-2006 observed time series of APF before computing the correlograms shown later in this section.

10   **3.2 Influence of large-scale climate modes on observed streamflow at Fraser-Hope**

We begin by examining the influence of the PDO and ENSO on the observed APF at the Fraser-Hope stream gauge station. This station was not included in the Gurrapu et al. (2016) study, but we derive results similar to theirs at other stations, as shown in Fig. 2. The figure shows that higher APF is associated with negative (cold) phases of the NINO3.4 (Fig. 2a) and PDO (Fig. 2b) indices over the 103-year record (1912-2014) at Fraser-Hope. While the statistical relationships between the

15   large-scale climate modes and the APF are robust (Spearman correlation of $\hat{\rho} = -0.40$ for NINO3.4, $\hat{\rho} = -0.35$ for PDO, both with $p < 10^{-3}$), Figs. 2a and b show that the largest APF in the record (1948; shown in boldface font on the plot) occurred during a neutral PDO phase and weak La Niña conditions, as did the fifth- and sixth-largest (1964 and 1997, also in bold). The second- to fourth-largest APFs (1972, 1950, 2012) occurred during strong negative PDO phases but weak La Niña conditions. This suggests that while APFs occurring during a negative PDO or La Niña phase may be larger than average,

20   the very largest APFs may be influenced by more local drivers, of either climatic or non-climatic nature (e.g., elevation and aspect). Indeed, our results indicate that the PDO and NINO3.4 indices explain only ~ $\hat{\rho}^2$ ~ 0.12−0.16 or 12−16% of the variance (with considerable interdependence between the two modes). Correlations of similar magnitude and sign were found at many more stations within the FRB by Thorne and Woo (2011).

Another way of visualizing streamflow sensitivity to ENSO and PDO phase is exhibited in the quantile plots of Fig.

25   2c and d. A quantile plot can reveal differences in sample distributions more clearly than a histogram or density plot (Coles et al., 2001). For example, for the PDO the time series of APF was first divided into years with positive (PDO$_{pos}$) and negative (PDO$_{neg}$) PDO index. Then a resampling (permutation) test was applied to check whether the test statistic $S =$ [mean(APF)]$_{PDO,neg}$/[mean(APF)]$_{PDO,pos}$ differed from that calculated from 10^4 random samples of the combined (both positive and negative PDO phase) data set. Fig. 2d shows that the APF in years with negative (cold) PDO phase is

30   significantly larger than in years with positive (warm) PDO phase, consistent with the relationship seen in the scatter plot (Fig. 2b). Similar results were found for ENSO, as seen in Fig. 2c.

3.3 Basin-scale relationships amongst observed variables

We begin our investigation of basin-scale drivers for APFs by looking again at the observed data. Specifically, we regressed the observed APF at Fraser-Hope against FRB-wide averages of the observed predictors in Table 2. Fig. 3b shows a correlogram of the univariate regression results for all observed variables over the common period of 1956-2006. Variables with detected trends over this period (Sec. 3.1) were also detrended before constructing the corelogram, as described in Sec. 2.3. We summarize the results for individual predictors below, before looking at their joint influence on APF at the end of the subsection.

3.3.1 Snow water equivalent (SWE)

As expected given the mainly nival character of the FRB, we find that interannual variations in April 1 SWE and APF are strongly correlated, with a Spearman correlation of $\hat{\rho} = 0.64$ over the common period of 1956-2014 of the MSS and WSC time series (Fig. 3a). This figure shows the raw data, while Fig. 3b shows the correlogram of all variables over the shorter common period of 1956-2006, including detrending where necessary. These differences lead to a somewhat smaller $\hat{\rho} = 0.51$ between April 1 SWE and APF. Nevertheless, the conclusion that years with higher than average SWE tend to produce higher peak streamflow at Fraser-Hope remains robust.

3.3.2 Temperature

Several diagnostics of the effect of surface air temperature T on APF were examined. First, we computed the absolute value of the sum of negative daily mean $T < 0$ °C from October 1 – March 31, or freezing degree days (FDD), from the PCIC-OBS data averaged over the entire FRB. This helps determine whether exceptionally cold winters lead to an unusually large snowpack, potentially producing an enhanced snowmelt contribution to the spring freshet. Second, we calculated the April-June mean temperature T_{amj}, which roughly coincides with the interval between the time of April 1 SWE and APF. Finally, we computed the warming rate over the freshet period, dT/dt, by computing the linear least-squares slope of T between April 1 and the date of APF. Over the 1956-2006 period at Fraser-Hope, the date of APF ranges from May 16 to July 23, with a median of June 13. The corresponding warming rates in different years range from 0.093 to 0.26 °C day^{-1} (median = 0.16 °C day^{-1}), implying a typical warming over the median freshet (under the linear approximation) of ~ 11 °C.

The correlations of these variables with APF are displayed in the correlogram of Fig. 3b. Here it is seen that amongst these variables, April-June mean temperature is anti-correlated with APF ($\hat{\rho} = -0.42$), while FDD and dT/dt are positively correlated with APF [$\hat{\rho} = 0.21$ (not significant) and $\hat{\rho} = 0.26$, respectively]. All else being equal, an unusually cold winter (high FDD) would be expected to result in a larger snowpack and a larger snowmelt contribution to streamflow consistent with the positive correlation found between FDD and APF. By the same reasoning, an unusually cold spring (low T_{amj}) resulting in a delayed, but more rapid snowmelt during the freshet, would again be expected to increase that year's APF. In years with normal summer T, this situation would produce a larger than normal warming rate, consistent with the

positive correlation found between dT/dt and APF. Finally, we note from Fig. 3b that a positive correlation is seen between T_{amj} and dT/dt ($\hat{\rho} = 0.30$), implying that high spring temperatures are associated with rapid warming.

3.3.3 Rainfall

While the snowfall portion of precipitation P accumulates as SWE, whose effect on APF was examined above, it is also
5   desirable to estimate the rainfall-only portion, R. We do this using the empirical fit of Dai (2008), which relates the fractional rain frequency to surface temperature via a hyperbolic tangent function having four fitted parameters. We chose the parameter values corresponding to land-only, annual mean precipitation (seasonal fitted coefficients were also given by Dai [2008], but do not differ much from the annual values). Daily rainfall R shows a high temporal variance even when averaged over the entire FRB, which could introduce spurious noise into the regressions. For this reason, we looked at three integrated
10 forms of R: 1) the summed rainfall over the winter months, $R_{Oct-Mar}$; 2) the sum of rainfall between April 1 and the day of APF, R_{Spring}; and 3) the sum of R over a period from 15 days in advance to 5 days after the day of peak streamflow, R_{APF}. These three metrics offer differing probes of the influence of rainfall on the APF at increasing temporal resolution.

None of the above rainfall measures displayed a significant relationship with observed APF (Fig. 3b), reinforcing the designation of the FRB as a primarily nival basin. Indeed, R_{APF} was completely unrelated to APF ($\hat{\rho} = 0.02$, not shown in
15 Fig. 3b). Although severe flooding in several small catchments in the U.S. Pacific Northwest has been attributed to rain-on-snow events (McCabe et al., 2007; Surfleet and Tollos, 2013), we see no evidence of this in the much larger FRB.

To better identify significant, multi-day rainfall episodes, we computed an index of past and current rainfall, the current rainfall index, or CRI, that reflects both antecedent and current rainfall inputs: $CRI_t = K \times CRI_{t-1} + R_t$. Here R_t is the basin-averaged precipitation for day t and K is the daily recession coefficient, set equal to 0.9 following previous studies
20 (Fedora and Beschta, 1989; Smakhtin and Masse, 2000). Unlike SWE, the basin-averaged, annual maximum CRI, CRI_{max}, generally occurs during summer, although multiple peaks in a given year are often observed (see ff., Fig. 9). Computing CRI_{max} from the daily time series, we find a broad distribution ranging over the later half of the year, i.e. calendar days 160 to 301. This contrasts with the narrower distribution of APF dates occurring in spring-summer (days 136-204), suggesting a weak relationship between the two on the seasonal time scale.

25 To investigate the influence of rainfall on streamflow more generally, we interrogated the respective deseasonalized daily time series. Specifically, we computed the annual cross-correlation function between streamflow (X) and CRI (Y) anomalies for each year i:

$$\hat{\rho}_{XY,i}(\tau) = \frac{\text{mean}[X'_i(t)Y'_i(t+\tau)]}{\hat{\sigma}_{X,i}\hat{\sigma}_{Y,i}}$$

where $X'_i(t)$ is the anomaly time series of X (i.e. difference between X and its multi-year mean annual cycle) in year i, $\hat{\sigma}_{X,i}$ is
30 the standard deviation of X'_i (and similarly for Y), and τ is the applied lag between X'_i and Y'_i, ranging over ±183 days. If $\max(\hat{\rho}_{XY,i}) > \delta$ at $\tau > 0$, where $\delta = 2/\sqrt{N} = 2/\sqrt{365}$, then CRI both leads and positively correlates with streamflow in that

year, suggesting a causal relationship. The results show that about half (26 of 50) of the years exhibit a significant relationship at some time during the year, with $\max(\hat{\rho}_{XY,i})$ ranging from 0.24−0.72 with lags of $\tau = 0$-51 days (Fig. 4, open circles). Two clear outliers, at $\tau = 93$ and 114 days, were disregarded. It can be seen in Fig. 4 that three out of the five (and four of the ten) largest correlations were associated with strong El Niño years, each with a lag of 2 days or less between

5 rainfall and streamflow. Rainfall events in the upper reaches of the FRB can have a delayed effect on streamflow at Hope of up to ~1 week (BC River Forecast Centre, 2012), while in years with $\tau = 1$ to 8 weeks, soil moisture that is near field capacity might be responsible for successive overland flow following rainfall events. However, Fig. 4 shows that these situations tend to occur during weak or moderate La Niña conditions.

Finally, we note the possibility that significant multi-day rainfall events coinciding with frozen or saturated soils

10 might lead to occasional flooding at local scales within the FRB. While suitable soil moisture observations are not readily available at this time (see Sec. 5), we employ the VIC model to examine the role of soil moisture in both the FRB and its sub-basins using the regression framework in Section 3.4.

3.3.4 Relationships amongst observed predictors

Finally, we investigated relationships amongst observational variables unrelated to streamflow revealed in the

15 correlogram of Fig. 3b. April-June mean temperature is positively correlated with spring warming rate and negatively correlated with April 1 SWE, both intuitively reasonable results, as is the positive correlation of FDD with April 1 SWE. Strong inverse relationships also exist between spring rainfall and: (i) T_{amj} ($\hat{\rho} = -0.48$), and (ii) warming rate ($\hat{\rho} = -0.69$). Both of these relations are reasonable given that the rainfall fraction diminishes approximately linearly with decreasing temperature toward 0 °C, according to the Dai (2008) parameterization used here. Finally, cold season (Oct-Mar) rainfall is

20 anti-correlated with FDD ($\hat{\rho} = -0.32$) (Fig. 3b).

3.3.5 Multivariate regression

The above results were derived using univariate linear regression and correlations computed using the Spearman rank method. However, we also would like to attribute interannual variance in the APF to the combined variances of the predictors. As described in Sec. 2.3, we constructed a number of MLR relations including all possible combinations of the

25 above variables that showed a significant Spearman $\hat{\rho}$ when regressed individually against APF.

The MLR procedure yields the following multilinear regression fits:

$$\widehat{APF}_{obs} = 4535 + 11.40\ \text{SWE}_{\text{Apr1}} + 17068\ (dT/dt) - 603.2\ T_{\text{amj}} \qquad (R_{\text{adj}}^2 = 0.63, p < 10^{-9}) \qquad (1)$$

$$\widehat{APF}_{obs} = 4106 + 10.48\ \text{SWE}_{\text{Apr1}} + 17815\ (dT/dt) - 494.3\ T_{\text{amj}} - 402.3\ \text{NINO3.4} \quad (R_{\text{adj}}^2 = 0.65, p < 10^{-9}) \qquad (2)$$

Eq. (1) includes only local, basin-averaged predictors, while Eq. (2) includes the non-local influences of ENSO and PDO. Interestingly, only NINO3.4, not the PDO index, is a significant predictor of APF in the MLR, despite the comparable importance of both indices in the univariate regressions (Sec. 3.2). Additional parameters of the fits are summarized in Table 4. The predictors on the right-hand side of Eqs. (1) and (2) are ordered from left to right by decreasing partial F value: e.g.,

5   SWE_{Apr1} contributes the majority of the interannual variance in APF, followed by dT/dt, T_{amj} and NINO3.4 (Table 4). Together, these variables explain 65% of the variance, 2% more than if the influence of ENSO is ignored. As mentioned above, rainfall variables do not contribute significantly to the interannual variability of the observed APF at Fraser-Hope.

3.4 Observed versus VIC-simulated streamflow and SWE

10   Before exploring relationships between APF and the wider array of variables available in the VIC hydrological model, as an evaluation exercise we compare several features of the VIC simulations with available observations in the FRB. In Fig. 5a, we compare the ten largest APFs in observations and VIC at Fraser-Hope station over the simulation period of 1955-2004. The APFs have been ranked by their observed magnitude, with the highest flow years at the left-hand side of the bar graph. In most years, the VIC-simulated APFs are close to the observed values. Fig. 5b compares the daily climatology and

15   interannual variability of VIC and observations for all years. VIC tends to overestimate the magnitude of the APF by ~8% (multi-year mean) to 16% (multi-year maximum), and also simulates an annual peak flow date (APD) ~5 days later than in the observations. VIC underestimates interannual streamflow variability over most of the year, except over the period of peak flow from June to mid-August, when it displays higher variability.

Fig. 5c shows quantile plots of APF and APD for VIC compared to observations over the 1956-2006 period. Here,

20   the permutation test was applied using the test statistic $R = [mean(APF)]_{VIC}/[mean(APF)]_{OBS}$ (Sec. 3.1). Fig. 5c shows that for both APF and APD, the high bias in the VIC-OBS simulated APF is distinguishable from the stream gauge observations at the ~7% significance level (i.e. only 7% of the R values calculated from the resampled data were larger than the original R), while the late bias in APD is significant at the ~1% level. If the two outliers with VIC-simulated APF greater than 13,000 $m^3 s^{-1}$ are removed, the simulated and observed distributions are indistinguishable ($p = 0.24$). As our main concern in this

25   work is with identifying key predictors of the APF, with less emphasis on APD, we conclude that VIC does a reasonable job of simulating APF compared to observations.

Due to the dominant influence of annual snowpack on APF, it is also desirable to compare the VIC-simulated SWE with observed April 1 SWE measurements. Although the version of VIC used here does not simulate glacier physics, the model produces a perennial, accumulating snowpack at several high-elevation grid cells (also noted by Islam and Déry,

30   2017). These anomalous cells cause the annual maximum of the basin average SWE, SWE_{max}, to increase approximately linearly with time. In the analysis of the VIC-OBS simulation, we use SWE_{max} as a predictor instead of SWE_{Apr1} since it is expected to be more closely linked to APF on physical grounds. The linear increase in SWE_{max} is clearly unrealistic and is not seen, e.g., in the corresponding observed April 1 SWE time series, which has a trend indistinguishable from zero.

Therefore, we masked out these "glacier cells" according to the criterion $d[SWE_{max}(i, j)]/dt < 60$ mm y^{-1}, where $SWE_{max}(i, j)$ is the annual maximum value at grid cell (i, j) and the trend is calculated using a linear least squares fit over the 1950-2006 period of the VIC-OBS simulation. The threshold value of 60 mm y^{-1} was chosen to yield a basin average SWE_{max} trend of zero, in agreement with the observations. In addition, we confirmed a posteriori that the removal of these anomalous cells

5 has little effect on the correlation structure of the basin average SWE_{max} with any of the variables examined below.

In Fig. 5d, the annual cycle of the corrected, VIC-simulated SWE is compared with the observed April 1 SWE, with both quantities represented by their basin averages. While VIC-OBS clearly underestimates the observed April 1 SWE, there is significant overlap in the interannual ranges of simulated and observed peak annual SWE. Schnorbus et al. (2010) pointed out that in the FRB, VIC tends to underestimate SWE_{max} and overestimate peak melt rate. Thus, despite the low bias in

10 SWE_{max}, this compensatory behaviour leads to the above-noted slight overestimate of the APF. In addition, we note that the VIC-OBS biases in peak streamflow and SWE over the FRB are qualitatively consistent with VIC simulations over other nival basins (Salathé et al., 2014).

3.5 Relationships amongst VIC-simulated variables

15 In this section we apply the methodology of Sec. 3.3 to probe relationships amongst the wider array of variables available in the VIC hydrological model over the FRB. We begin with an analysis of the routed model streamflow at Fraser-Hope, as a representative outlet of the entire FRB, before examining VIC-modelled discharge at the outlets of four subbasins within the FRB in Section 3.6.

In addition to the PCIC-OBS variables used in the regression analysis of Sec. 3.3—which were used as daily

20 forcings for the VIC simulation—we include a number of variables available in the model but not in observations, namely: annual maximum of SWE averaged over the FRB, SWE_{max}; calendar date of SWE_{max} ; snowmelt rate, $d(SWE)/dt$; melt season length, SWE_{len}; and antecedent total column soil moisture (detailed definitions are given in Table 2). The regression results are again summarized as a correlogram (Fig. 6) and in Table 4. The annual snowmelt rate, $d(SWE)/dt$, was calculated as the best-fit, least squares linear slope of SWE between the dates of SWE_{max} and APF. Formally speaking, $d(SWE)/dt$ is

25 the snow ablation rate, which in VIC includes snowmelt as the dominant contribution along with evaporation and rain-on-snow (other snow removal processes occurring in nature such as blowing snow, avalanches, etc. are not simulated). For convenience, however, we refer to $d(SWE)/dt$ as simply the snowmelt rate with the understanding that these other processes may make minor contributions to snowpack disintegration.

3.5.1 Influence of large-scale climate modes on streamflow at Fraser-Hope

30 Through the influence of the forcing variables, the PDO and ENSO may affect the VIC-simulated APF at Fraser-Hope. Indeed, we find a slightly more robust, but qualitatively similar, relationship between the large-scale climate indices and

modelled APF than for observed APF: as seen in Fig. 6, the correlations are Spearman $\hat{\rho} = -0.41$ for NINO3.4 and $\hat{\rho} = -0.38$ for PDO (both at $p < 10^{-2}$).

3.5.2 Snow water equivalent and snowmelt

As found for the observed April 1 SWE, we find that SWE_{max} exercises a strong control on APF ($\hat{\rho} = 0.70$, $p <$
5   0.001; Fig. 6). The latter lags SWE_{max} by an average of 84 days (range 52-127 days) over the simulation period; examples for specific years are displayed in Fig. 9. Further, Table 5 shows that of the top ten APF years in this period, seven were in the top ten of SWE_{max}. Yet, the highest APF corresponds to the 6th-largest SWE_{max} (1982), while the 4th-highest APF occurred in an average year for snow accumulation (1958). It is therefore of interest to investigate what conditions, independent of snow accumulation, led to the comparatively large APF in those years.

10   Snowmelt displays significant positive correlations with APF ($\hat{\rho} = 0.43$) and several other predictors, namely: SWE_{max} ($\hat{\rho} = 0.63$), FDD ($\hat{\rho} = 0.38$), date of SWE_{max} ($\hat{\rho} = 0.32$), dT/dt ($\hat{\rho} = 0.25$), and maximum annual soil moisture ($\hat{\rho} = 0.64$). Significant negative correlations are also found with melt season length ($\hat{\rho} = -0.53$) and the NINO3.4 and PDO indices ($\hat{\rho} = -0.28$ and -0.46, respectively). In years with high SWE_{max}, initial snowmelt in spring recharges soil moisture (over unfrozen ground; see Sec. 3.5.3), which in turn aids further melting, leading to the strong positive correlation seen in
15   VIC. The inverse relationship with the large-scale indices should be considered in light of their similar relationship with SWE_{max} ($\hat{\rho} = -0.47$ and -0.62, for NINO3.4 and PDO respectively): higher snowpack accumulates during La Niña and negative PDO phases, with reduced snowmelt due to cooler temperatures.

3.5.3 Soil moisture

In our VIC simulation, the basin-averaged annual peak soil moisture, SM_{max}, occurs during the snowmelt period
20   from mid-March to mid-June, most often near the end of May, well after the day of SWE_{max} and approximately 3 weeks in advance of the APF (for an illustration depicting individual years, see Fig. 9). The direct influence of both SWE_{max} ($\hat{\rho} = 0.83$) and snowmelt ($\hat{\rho} = 0.64$) on SM_{max} is detected at high confidence ($p <$), while SM_{max} is, in turn, strongly correlated with APF ($\hat{\rho} = 0.65$, $p <$) in the annual time series (Fig. 6). A cross-correlation analysis of the respective daily time series over the entire common period reveals that, on average, SWE leads SM by 68 days (maximum cross-correlation, $R = 0.65$),
25   SM leads streamflow by 22 days ($R = 0.85$), and SWE leads streamflow by 105 days ($R = 0.74$). The higher cross-correlation between SM and streamflow indicates that the annual cycle of SM is a better predictor of the daily streamflow hydrograph than SWE, despite the above-mentioned superiority of SWE_{max} as an annual predictor of APF. This is a reasonable result, since during the freshet, daily SM integrates contributions from both snowmelt and precipitation. On the other hand, SM_{max} could be considered inferior to SWE_{max} as a predictor of APF with respect to its much shorter lead time. SM_{max} also exhibits
30   significant relationships with FDD ($\hat{\rho} = 0.33$), T_{amj} ($\hat{\rho} = -0.27$), and the NINO3.4 and PDO indices ($\hat{\rho} = -0.44$ for both). The negative phases of ENSO and the PDO bring more rain and snow, which consequently enhances soil moisture.

Also of interest is a possible relationship between APF and SM preceding the snowmelt period, for example, in fall before snow accumulation begins. Numerous studies point to the influence of antecedent soil moisture on seasonal streamflow in nival catchments (Maurer and Lettenmaier, 2003; Berg and Mulroy, 2006; Williams et al., 2009; Harpold and Molotch, 2015). Using a suite of land surface models including VIC, Koster et al. (2010) and Mahanama et al. (2012) demonstrated improvement of March-July streamflow forecast skill over the western United States using antecedent (January 1) soil moisture in addition to snow amount as a predictor. The basic mechanism is that antecedent reduced storage capacity of wet or frozen soils leads to more of the snowmelt being routed to discharge during the spring freshet, and vice-versa for dry soils. To investigate the interannual sensitivity of APF to antecedent SM, we used monthly mean SM from the preceding August through November in turn as predictors of APF, but found no significant correlations. This insensitivity may be due to the lack of a frozen soil parameterization in the version of VIC used here. In this implementation, soil drainage over the cold season tends to be overestimated (Cherkauer and Lettenmaier, 2003), which could cause a decoupling between autumn SM and spring freshet flows.

3.5.4 Temperature and rainfall

As in the observations, FDD and spring warming rate dT/dt are positively correlated with APF ($\hat{\rho} = 0.24$ and $\hat{\rho} = 0.38$, respectively; Fig. 6). The connection between dT/dt and APF is stronger than in the observations but, interestingly, there is no significant correlation between T_{amj} and APF as exists in the observational data (Eq. [1] and [2]).

Again as in the observations (Sec 3.3.3), no significant correlations are found between any of the rainfall measures and VIC-simulated APF. However, as also found in the observations, there are indications of a rainfall-streamflow connection at other times of the year. Repeating the cross-correlation analysis between streamflow and CRI as in Sec. 3.3.3 reveals that 20 of 50 years exhibit a significant relationship at some time during the year, with max($\hat{\rho}_{XY,i}$) ranging from 0.27−0.66 with lags of $\tau = 2$-55 days. Two clear outliers, at $\tau = 91$ and 142 days, were disregarded. Fig. 4 (triangles) shows that most (9) of the rainfall-influenced years occur during the El Niño phase, while 4 occur during La Niña and 7 during neutral years. Twelve of the 20 rainfall-influenced years occur during the cool phase of the PDO. More often than not, however, CRI lags daily streamflow, suggesting little to no relationship. With regard to other relationships, we find that cold season rainfall is correlated with spring rainfall ($\hat{\rho} = 0.32$) and anti-correlated with FDD ($\hat{\rho} = -0.32$) (Fig. 6). As mentioned in Sec. 3.3.4, spring rainfall is negatively correlated with T_{amj}, dT/dt, and snowmelt, but with slightly different $\hat{\rho}$ values due to the different lengths of averaging period in the calculations compared to the observed case (as per the definitions in Table 2).

3.5.5 Multivariate regression

As in the case of the observed variables, we constructed MLR relations including all combinations of the variables in Fig. 6 that showed a significant Spearman $\hat{\rho}$ and selected the optimal MLR based on the criteria specified in Sec. 3.3.5. One predictor that was excluded from the MLR was SM_{max}: its high correlation with SWE_{max} indicates that its independent

5   explanatory power is limited (Sec. 3.5.3). The resulting relationship is:

$$\widehat{APF}_{VIC} = 3239 + 37.14 \, SWE_{max} + 26842 \, (dT/dt) - 57.69 \, SWE_{len} + 1770 \, d(SWE)/dt \qquad (R_{adj}^2 = 0.75, \, p < 10^{-9}) \qquad (3)$$

In contrast to the MLR constructed for observed streamflow, Eq. (2), neither of the large-scale climate indices has a

10   significant influence, nor is T_{amj} an important predictor. Nevertheless, the four variables on the right-hand side of Eq. (3) account for 75% of the interannual variance in APF. Three of the four were identified in the univariate regressions as important, with the exception being the length of the melt season, SWE_{len}. The latter displays a strong anti-correlation with snowmelt ($\hat{\rho} = -0.55$, Fig. 6), suggesting that the two variables are not independent. However, since removing each of SWE_{len} and $d(SWE)/dt$ from the MLR in turn yields a significantly poorer fit ($R_{adj}^2 = 0.71$ for $d(SWE)/dt$ only and $R_{adj}^2 =$

15   0.69 for SWE_{len} only), it seems that both predictors have some explanatory value. The absence of both the PDO and NINO3.4 indices from the MLR could be a reflection of the limitations of the driving data, inasmuch as the processing of gridded station data to the regular grid may weaken the influence of the large-scale climate drivers (Sec. 2.1).

3.6 Relationships amongst VIC-simulated variables at the subbasin scale

The same analysis as conducted for the entire FRB was repeated for each of the four subbasins comprising more than 70% of

20   the annual flow at Fraser-Hope (Table 1). The results of the univariate regressions are presented as a correlogram in Fig. 7 while those for the MLR are provided in Table 4.

Overall, the relationships in the subbasins mirror those seen in the FRB as a whole. The univariate analysis shows that in all four subbasins, SWE_{max} and SM_{max} are good predictors of APF, while snowmelt and FDD exhibit positive correlations with APF in three of the four subbasins, Chilko being the exception (Fig. 7). While SWE_{max} has a slightly

25   stronger influence on APF than SM_{max} in the FRB, SM_{max} is more influential at the subbasin scale, explaining over 75% of the variance in APF in Quesnel (compared to 40% for SWE_{max}). Spring dT/dt and APF are strongly correlated in Thompson-Nicola and weakly in Quesnel. Three of the four subbasins exhibit a strong inverse relationship between APF and the NINO3.4 and PDO indices, again with the exception of Chilko. The weak dependence of streamflow on the PDO, SOI and Pacific-North American indices in this and other catchments in the western FRB was also noted by Thorne and Woo (2011).

30   The insensitivity of APF to the local, basin-averaged predictors might be related to the smaller size of the Chilko compared to the other three subbasins, which lowers the signal-to-noise ratio of the basin averages. This, along with the comparatively

lower APFs at the basin outlet, makes the detection of significant correlations more challenging in Chilko compared with the other subbasins.

Moving now to the MLR analysis, the results in Table 4 demonstrate that in all four subbasins, SWE_{max} is the most skillful predictor of APF, again in agreement with the results for the FRB as a whole. Likewise, in three of the four

5 catchments, dT/dt emerges as the next most significant variable. The exception is the Upper Fraser basin, where SWE_{len} is the second most skillful predictor. In this subbasin, APF is inversely correlated with SWE_{len} in the MLR, while the latter is in turn anti-correlated with both dT/dt ($\hat{\rho} = -0.81$, $p < 0.05$) and T_{amj} ($\hat{\rho} = -0.25$, $p < 0.1$) in the univariate regressions (Fig. 6). These results suggest that anomalously warm springtime temperatures (compared to the preceding winter) are at the heart of the APF-SWE_{len} relationship in the Upper Fraser, not unlike what is seen in the other subbasins.

10 In contrast to the FRB as a whole, rainfall does appear to have a weak influence on APF in two of the subbasins. However, in each subbasin, APF is sensitive to a different measure of rainfall. In Thompson-Nicola, the basin with the largest area and second-highest mean elevation, $R_{Oct-Mar}$ is positively correlated with APF, while in the Upper Fraser, R_{Spring} displays a somewhat weaker positive relationship to APF. In the Quesnel, a smaller basin of lower mean elevation, the preceding September mean soil moisture is an effective predictor of APF. Interestingly, neither the NINO3.4 nor the PDO

15 index is an effective predictor of APF in the MLR of any of the subbasins, despite the fact that strong inverse relationships are still seen in the univariate correlogram (Fig. 6).

3.7 Co-dependence of streamflow predictors

The above results make clear that, of the predictors considered in the FRB and its subbasins, APF is primarily influenced by SWE_{max} and the rate of warming in spring, dT/dt. To further explore this co-dependence, we show in Fig. 8 a scatterplot of

20 the relative anomaly of each of these two predictors, $(X_i - \overline{X})/\overline{X}$, where X_i is the value of predictor X at year i and $\overline{X}$ is the long-term mean (1955-2004), with the corresponding streamflow relative anomaly $\Delta Q/\overline{Q}$ indicated by the point colour. This type of plot has been used previously to explore the elasticity (i.e., non-linearity) of streamflow as a function of covariates (e.g., Andréassian et al., 2016). However, here we employ it primarily as an additional illustration of the co-dependencies identified by the MLR analysis.

25 In the FRB, the roughly uniform pattern of scatter in the vertical and horizontal directions indicates a weak co-dependence between ΔSWE_{max} and $\Delta dT/dt$, consistent with expectation—dT/dt is computed only after the day of SWE_{max} each year—and with the results of Figs. 5 and 6. The corresponding $\Delta Q/\overline{Q}$ values display an overall gradient from bottom left to top right, i.e. from lower than average SWE_{max} and dT/dt to higher than average SWE_{max} and dT/dt, again consistent with the univariate and multivariate regression results. Qualitatively similar results are found in the Chilko, Thompson-

30 Nicola and Quesnel subbasins.

In the Upper Fraser subbasin, the primary predictor is still SWE_{max} but the secondary predictor is SWE_{len}. As a result, the scatterplot displays a weak co-dependence between relative changes in the two variables, with some clustering

toward the diagonal. Furthermore, the overall gradient in $\Delta Q / \overline{Q}$ is from top left to bottom right, i.e. from lower than average SWE_{max} and higher than average SWE_{len} to higher than average SWE_{max} and lower than average SWE_{len}. That is, in years when an anomalously large snowpack ($\Delta SWE_{max} > 0$) melts fairly quickly ($\Delta SWE_{len} < 0$), streamflow tends to be larger than usual ($\Delta Q > 0$).

4 Case studies: High-flow years in the FRB

While the MLR approach captures the relationship between various predictors and APF in the FRB and its subbasins in a statistical manner, it can miss unusual weather factors that are important in specific years. For this reason, we present in this section an "anatomy" of streamflow and the associated key hydrological variables in years of particularly high

10   VIC-simulated discharge at the Fraser-Hope station. We focus on VIC-simulated variables since full time series of all variables of interest are available to construct both a climatology and annual cycles for specific years.

Table 5 shows the top ten APFs occurring in the VIC simulation from 1955-2004, with corresponding rankings of other key predictors entering the regression analysis of Sec. 3. Seven of the top ten SWE_{max} years are in this group. This highlights the dominant effect of spring snowpack on APF magnitude in the FRB. A similar result holds for observed basin-

15   averaged April 1 SWE and APF at Fraser-Hope: eight of the top ten April 1 SWE years are also amongst the top ten observed APFs. Looking at results for the other predictors, seven of the top ten SM_{max} years (not surprising given the linkage between SWE_{max} and SM_{max} noted in Sec. 3.4.3), four of the top ten spring warming rates and three of the top ten FDDs are in the group of top ten APFs. Only one of the top ten spring rainfalls is in the group, which happens to be the highest simulated rainfall in 1999 (8th largest APF). These results are therefore consistent with the key predictors identified for APF

20   in the regression analysis of Sec. 3.

Fig. 9 shows the annual cycle of discharge at Fraser-Hope along with other variables of interest over the calendar year for three of the top ten APF years: 1958, 1972 and 1999. The daily evolution of discharge Q at Fraser-Hope and basin-averaged SWE, T, CRI and SM are plotted, along with their 1955-2004 climatologies, as an aid to evaluating how anomalous a given year is. A 15-day smoothing filter was applied to T to better highlight sub-seasonal trends. Also shown in the bottom

25   two subpanels of each panel are the difference between the slope of T calculated over a 61-day moving window in the year of interest and its climatology (the warming rate anomaly), and the difference of the snowmelt rate from its climatology calculated over a 15-day moving window. Both anomalies were set to zero if $T < 0$, since we are interested in behaviour during the melt season only. We consider each year in turn, as each exhibits a unique phenomenology that illuminates the development of the APF in that year.

4.1 Warm spring in an average SWE year: 1958

APF in the year 1958 ranked fourth over the 1955-2004 period of the simulation (Table 5). Yet, as simulated by VIC, 1958 was a normal SWE year, with SWE_{max} achieved near the end of March. Rainfall and soil moisture were also near normal up to this point, while winter temperatures were above normal but still below freezing (Fig. 9a). At the beginning of

5   the melt season in April, dT/dt began to exceed its climatological value, prompting rapid snowmelt toward the end of that month. The anomalous snowmelt persisted until the end of May, about the time of the APF (APD), while the period of elevated warming rate continued into early June. The snowmelt pulse produced a coincident soil moisture anomaly, which is remarkable in that these quantities are averaged over the entire FRB, yet their behaviour is consistent with small-scale processes. Subsequent to the APD, the soil moisture anomaly became negative, apparently in response to the prolonged

10   warming, which would lead to enhanced evaporation, and lower than normal rainfall over the summer. Fig. 9a demonstrates that neither rainfall nor high soil moisture prior to freeze-up were pivotal factors in producing the anomalously large APF in this year. Indeed, rainfall amounts were well below normal between snowmelt initiation and the APD (49th out of 50 years; Table 5).

15   ### 4.2 Influence of rainfall in a high-SWE year: 1972

The second-highest simulated APF over the 1955-2004 period occurred in 1972, which also featured the second-highest SWE_{max} (Table 5). This year also exhibited the largest observed APF over the same period (Fig. 5a). While the preceding winter was colder than normal—evidently a factor in generating an anomalously large snowpack—the spring warming rate was above-normal, resulting in a strong snowmelt anomaly lasting from May until just after the APD in early

20   June (Fig. 9b). As in 1958, this snowmelt pulse generated a large soil moisture anomaly, which likely produced more overland flow during the freshet. This evidence suggests that the extreme APF in 1972 was primarily caused by a combination of elevated warming in spring and an abnormally large snowpack, which provided a large water surplus during the freshet. However, there is also an indication that a series of heavy rainfall episodes starting in early June, just days before the APD, affected the APF and particularly the duration of the high-flow period. An extended period of anomalously large

25   rainfall is seen in the CRI between early June and late July, with a clear response in SM and in the persistence of the high-discharge anomaly until the end of August—both are clearly distinguishable from their counterparts in 1958 (Fig. 9a).

Finally, it is worth noting that 1982, the year with the highest simulated APF (not shown in Fig. 9), was characterized by a very similar evolution of predictors as in 1972, including an extended, coincident period of anomalously large rainfall. However, in that case, there were two additional elements: 1) the spring warming rate was the highest of any

30   year in the record (Table 5), and; 2) a strong warm anomaly ~+5 C occurred in mid-June just prior to the APD, which evidently generated enough additional snowmelt runoff to position that APF as the highest over the simulated period.

4.3 A rainfall-dominated APF: 1999

The year 1999 holds the distinction of having the highest simulated spring rainfall in the record. It also had the fourth-largest VIC-simulated SWE_{max}, while ranking eighth in APF (Table 5). The temperature development was unremarkable, however, if a little colder than the climatology in the freshet months of April and June (Fig. 9c). The

5   hydrograph reflects this increased role of rainfall by its evident synoptic time scale variability, in contrast its smoother counterpart in the snowmelt-dominated years examined above (Fig. 9a,b). Indeed, the character of the hydrograph over the freshet period is such that isolating the single largest APF misses key features of the flow development, which involves not one but four peak flows of roughly equal magnitude spanning the period from mid-June to mid-August. Consequently, the use of annual predictors with a single APF as predictand, as adopted in our univariate and multivariate regressions, is likely

10   to underweight a strong influence of rainfall in a particular year. Table 3 shows that the maximum cross-correlation of deseasonalized daily streamflow and CRI anomalies during 1999 is 0.61 at a lag of 35 days (CRI leading streamflow), while in 1958 the maximum is just 0.38 at a lag of 47 days. This implies that rainfall should be treated differently than SWE and other predictors in order to correctly capture its influence on APF. The evolution of SM is also different than in the prior cases considered, insofar as it displays step-like jumps in mid-March, early April, and mid-May followed by a plateau at a

15   high level until early July (Fig. 9c). This SM anomaly persisted for the remainder of the year, except for a brief two-week period in November. While in snowmelt-dominated years SWE approaches its climatological value in late summer (except in 1958, when it fell below that value), in 1999 a positive SWE anomaly persisted throughout the year.

5 Discussion and Conclusions

In Sec. 3.4, we showed that the VIC model driven by gridded observations provides an adequate simulation of streamflow

20   and maximum annual SWE in the FRB. The mutual resemblance of the correlograms (Figs. 3b and 6), which summarize the univariate linear regression fits to observed and VIC data, along with the similar forms of the respective MLR models (Eqs. [1]-[3]), give one further confidence in the ability of the VIC model to simulate interactions between the key controls of streamflow acting in the real system. Furthermore, differences in the key controlling variables in the observed and modelled cases suggest fruitful avenues of further research. For example, the use of more complete snow survey or satellite products

25   might permit the estimation of SWE_{len} or snowmelt rate, and confirmation of the influence of these terms appearing in the VIC-derived MLR, Eq. (3). Or conversely, improved driving data for the VIC model might reveal the influence PDO and/or ENSO explicitly in the MLR, or the inverse correlation with spring temperature and/or freezing degree days.

It is interesting to ask whether any of the relationships found in this study might aid attempts to forecast a flood-level APF weeks or possibly months ahead of the freshet period. Although based on only 50 years of simulated basin

30   hydrology driven by observed data, the VIC results imply that a high SWE_{max}, say in the top quartile of historical values (i.e. 7 of the top ten in Table 5), increases the chance of an upper quartile APF. The long interval between SWE_{max} and APF, of order 2-4 months, makes the former a valuable early warning indicator of possible flooding in the lower FRB (BC River Forecast Centre, 2012). However, it is also true that three of the top ten SWE_{max} years (1976, ranked 3rd; 1991, 8th; and 1971,

9th) did not exhibit remarkable floods: in those years, the corresponding APFs ranked 20th, 30th and 23rd. And while SM_{max} has about the same success rate as a predictor of APF—seven of the top ten APF years are top ten SM_{max} years—these are the same as for SWE_{max}, meaning that soil moisture during the freshet is of little additional predictive value. As mentioned in Sec. 3.5.3, the lack of a connection between fall SM and APF in the historical VIC simulation suggests that future model
5   studies should include the effect of soil freezing, in order to more realistically simulate the spring thaw. Further, the estimation of groundwater storage and its evolution using NASA's Gravity Recovery and Climate Experiment (GRACE), which has proved promising for flood forecasting in large, snowmelt-dominated basins (Reager et al., 2014; Wang and Russell, 2016), could find useful application in the FRB.

In Section 3, we demonstrated that the springtime warming rate, dT/dt, was the next most skillful predictor of APF
10   in the regression analysis of Section 3. Moreover, dT/dt appears to provide additional predictive value over that of SWE_{max} and SM_{max}, insofar as two of the top ten dT/dt years are not top ten SWE_{max} and SM_{max} (1958 and 2002; Table 5). Thus, the combination of an upper quartile SWE_{max} with a high dT/dt over the snowmelt period may presage flooding at Fraser-Hope station (nine out of the top ten APFs were characterized by one or the other; four featured both). The definition of dT/dt used here is dependent upon the APD, which is of course unknown at the time of SWE_{max}; however, in a predictive context, one
15   could simply use the last daily T observation to compute the warming rate within a window of increasing duration. Finally, in the current climate we find little prospect of using basin-averaged, rainfall-related indices as predictors of APF at Fraser-Hope. It is possible, however, that at subbasin scales, and/or in combination with an appropriate soil moisture indicator, some measure of rainfall might prove useful for predicting localized flooding. This has been a valuable strategy for APF/APD hindcasting in nival-pluvial and pluvial catchments (Neiman et al., 2011; Surfleet and Tullos, 2013).

20   **Acknowledgements**

We thank Marcus Schnorbus and Arelia (Werner) Schoeneberg for helpful discussions regarding the VIC model, J. Cunderlik for sharing station locations from Cunderlik and Ouarda (2009), Faron Anslow for providing the regional temperature and precipitation time series data over British Columbia, and Siraj Ul Islam for comments that improved the manuscript. CC is supported by the NSERC-funded Canadian Sea Ice and Snow Evolution (CanSISE) Network.

25   **References**

Alexander, M.A.: Extratropical Air-Sea Interaction, SST Variability and the Pacific Decadal Oscillation (PDO), in: Climate Dynamics: Why Does Climate Vary?, D. Sun and F. Bryan (Editors). AGU Monograph #189, Washington, D.C., pp. 123-148, 2010.

Andréassian, V., Coron, L., Lerat, J. and Le Moine, N.: Climate elasticity of streamflow revisited-an elasticity index based
30   on long-term hydrometeorological records, Hydrol. Earth Syst. Sci., 20, 4503, 2016.

Bawden, A. J., Burn, D. H. and Prowse, T. D.: Recent changes in patterns of western Canadian river flow and association with climatic drivers. Hydrol. Research, 46, 551-565, 2015.

BC MOE, British Columbia Ministry of the Environment, Comprehensive Review of Fraser River at Hope Flood Hydrology and Flows—Scoping Study and Final Report, Northwest Hydraulic Consultants, available at:

5   http://www.env.gov.bc.ca/wsd/public_safety/flood/pdfs_word/review_fraser_flood_flows_hope.pdf, 2008.

BC MOE, British Columbia Ministry of the Environment: Indicators of Climate Change for British Columbia: 2016 Update. Available at: http://www2.gov.bc.ca/assets/gov/environment/research-monitoring-and-reporting/reporting/envreportbc/archived-reports/climate-change/climatechangeindicators-13sept2016_final.pdf, 2016.

Berg, A.A. and Mulroy, K.A.: Streamflow predictability in the Saskatchewan/Nelson River basin given macroscale estimates

10   of the initial soil moisture status, Hydrol. Sci. J., 51, 642-654, 2006.

Bonsal, B. and Shabbar, A.: Impacts of Large-Scale Circulation Variability on Low Streamflows Over Canada: A Review. Can. Water Res. J., 33,137-154, doi: 10.4296/cwrj3302137, 2008.

British Columbia River Forecast Centre, Flow Forecasting for the Lower Fraser River (from Hope to the Ocean), internal report, available at

15   http://bcrfc.env.gov.bc.ca/freshet/lower_fraser/Flow%20Forecasting%20for%20the%20Lower%20Fraser%20River.pdf
2012.

Burn, D. H. and Hag Elnur, M. A.: Detection of hydrologic trends and variability, J. Hydrol., 255, 107-122, 2002.

Cherkauer, K. A. and Lettenmaier, D. P.: Hydrologic effects of frozen soils in the upper Mississippi River basin. J. Geophys. Res.: Atmospheres, 104, 19599-19610, 1999.

20   Cherkauer, K. A. and Lettenmaier, D. P.: Simulation of spatial variability in snow and frozen soil. J. Geophys. Res.: Atmospheres, 108, doi:10.1029/2003JD003575, 2003.

Coles, S., Bawa, J., Trenner, L., and Dorazio, P.: An introduction to statistical modeling of extreme values, Vol. 208, Springer, London, 2001.

Coles, A. E., W. M. Appels, B. G. McConkey, and J. J. McDonnell: The hierarchy of controls on snowmelt-runoff

25   generation over seasonally-frozen hillslopes. Hydrol. Earth Syst. Sci. Discuss., doi:10.5194/hess-2016-564, 2017.

Cunderlik, J.M. and Ouarda, T.B.: Trends in the timing and magnitude of floods in Canada. J. Hydrol., 375, 471-480, 2009.

Dai, A.: Temperature and pressure dependence of the rain-snow phase transition over land and ocean, Geophys. Res. Lett., 35, doi:10.1029/2008GL033295, 2008.

DeBeer, C. M., Wheater, H. S., Carey, S. K., and Chun, K. P.: Recent climatic, cryospheric, and hydrological changes over the interior of western Canada: a review and synthesis. Hydrol. Earth Syst. Sci., 20, 1573, 2016.

Déry, S. J., Hernández-Henríquez, M. A., Owens, P. N., Parkes, M. W., and Petticrew, E. L.: A century of hydrological variability and trends in the Fraser River Basin, Environ. Res. Lett., 7, 024019, 2012.

5 Eaton, B. and R. D. Moore: Regional hydrology, in: Compendium of Forest Hydrology and Geomorphology in British Columbia, Pike, R.G., T.E. Redding, R.D. Moore, R.D. Winker and K.D. Bladon (editors), B.C. Min. For. Range, For. Sci. Prog., Victoria, B.C. and FORREX Forum for Research and Extension in Natural Resources, Kamloops, B.C. Land Manag. Handb. 66, www.for.gov.bc.ca/hfd/pubs/Docs/Lmh/Lmh66.htm, 2010.

Fedora, M.A. and Beschta, R.L.: Storm runoff simulation using an antecedent precipitation index (API) model, J. 10 Hydrol., 112, 121-133, 1989.

Fraser Basin Council: The Fraser: A Canadian Heritage River, 10-Year Monitoring Report. Available at: http://www.fraserbasin.bc.ca/resources_publications.html, 2010.

Gan, T. Y., Barry, R. G., Gizaw, M., Gobena, A., and Balaji, R.: Changes in North American snowpacks for 1979–2007 detected from the snow water equivalent data of SMMR and SSM/I passive microwave and related climatic factors. J. 15 Geophys. Res.: Atmospheres, 118, 7682-7697, 2013.

Gobena, A.K. and Gan, T.Y.: Low-Frequency Variability in Southwestern Canadian Streamflow: Links with Large-Scale Climate. Int. J. Climatol., 26, 1843-1869, doi: 10.1002/joc.1336, 2006.

Gurrapu, S., St-Jacques, J.-M., Sauchyn, D. J., and Hodder, K. R.: The Influence of the Pacific Decadal Oscillation on Annual Floods in the Rivers of Western Canada. J. Amer. Water Res. Assoc., 1-15. doi: 10.1111/1752-1688.12433, 2016.

20 Hamann, A., Wang, T., Spittlehouse, D.L., and Murdock, T.Q.: A comprehensive, high-resolution database of historical and projected climate surfaces for western North America, Bull. Am. Meteorol. Soc., 94, 1307–1309, 2013.

Harpold, A. A. and Molotch, N. P.: Sensitivity of soil water availability to changing snowmelt timing in the western U.S., Geophys. Res. Lett., 42, 8011–8020, doi:10.1002/2015GL065855, 2015.

Hernández-Henríquez, M. A., Sharma, A. R., and Déry, S. J.: Variability and trends in runoff in the rivers of British 25 Columbia's Coast and Insular Mountains. Hydrol. Process., 31, 3269–3282, 2017.

Islam, S. U. and Déry, S. J.: Evaluating uncertainties in modelling the snow hydrology of the Fraser River Basin, British Columbia, Canada, Hydrol. Earth Syst. Sci., 21, 1827-1847, doi:10.5194/hess-21-1827-2017, 2017.

Jenicek, M., Seibert, J., Zappa, M., Staudinger, M., and Jonas, T.: Importance of maximum snow accumulation for summer low flows in humid catchments, Hydrol. Earth Syst. Sci., 20, 859-874, 2016.

Jeong, D. I., Sushama, L., and Khaliq, M. N.: Attribution of spring snow water equivalent (SWE) changes over the northern hemisphere to anthropogenic effects. Climate Dynamics, 48, 3645-3658, 2017.

Kang, D.H., Gao, H., Shi, X., ul Islam, S. and Déry, S.J.: Impacts of a rapidly declining mountain snowpack on streamflow timing in Canada's Fraser River basin, Scientific Reports, 6, 19299, 2016.

5 Knowles, N.: Trends in Snow Cover and Related Quantities at Weather Stations in the Conterminous United States, J. Clim., 28, 7518-7528, 2015.

Koster, R.D., Mahanama, S.P., Livneh, B., Lettenmaier, D.P., and Reichle, R.H.: Skill in streamflow forecasts derived from large-scale estimates of soil moisture and snow, Nat. Geosci., 3, 613-616, 2010.

Liang, X., Lettenmaier, D.P., Wood, E.F., and Burges, S.J.: A simple hydrologically based model of land surface water and 10 energy fluxes for general circulation models, J. Geophys. Res., 99, 14415–14428, doi:10.1029/94JD00483, 1994.

Lohmann, D., Nolte‐Holube, R., and Raschke, E.: A large‐scale horizontal routing model to be coupled to land surface parametrization schemes, Tellus A, 48, 708-721, 1996.

Lohmann, D., Raschke, E., Nijssen, B., and Lettenmaier, D. P.: Regional scale hydrology: I. Formulation of the VIC-2L model coupled to a routing model, Hydrol. Sci. J., 43, 131-141, 1998.

15 Mahanama, S., Livneh, B., Koster, R., Lettenmaier, D., and Reichle, R.: Soil moisture, snow, and seasonal streamflow forecasts in the United States, J. Hydrometeor., 13, 189-203, 2012.

Maurer, E.P. and Lettenmaier, D.P.: Predictability of seasonal runoff in the Mississippi River basin. J. Geophys. Res.: Atmos., 108(D16), 2003.

McCabe, G.J., Clarke, M.P., and Hay, L.E.: Rain-on-snow events in the Western United States, Bull. Amer. Meteor. Soc., 20 88, 319-328, doi: 10.1175/BAMS-88-3-319, 2007.

Moore, R.D.: Hydrology and water supply in the Fraser River basin. Water in Sustainable Development: Exploring Our Common Future in the Fraser River Basin, A.H.J. Dorcey and J.R. Griggs (Editors). Westwater Research Centre, The University of British Columbia, Vancouver, British Columbia, Canada, 21-40, 1991.

Najafi, M.R., Zwiers, F., and Gillett, N.: Attribution of the Observed Spring Snowpack Decline in British Columbia to 25 Anthropogenic Climate Change, J. Climate, 30, 4113-4130, 2017.

Neiman, P.J., Schick, L.J., Ralph, F.M., Hughes, M., and Wick, G.A.: Flooding in western Washington: The connection to atmospheric rivers, J. Hydrometeor., 12, 1337-1358, 2011.

PCIC, BC Station Data PCDS, Pacific Climate Impacts Consortium. http://tools.pacificclimate.org/ dataportal/, last accessed July 21, 2016.

Pike, R. G., K. E. Bennett, T. E. Redding, A. T. Werner, D. L. Spittlehouse, R.D. (Dan) Moore, T. Q. Murdock, J. Beckers, B. D. Smerdon, K. D. Bladon, V. N. Foord, D. A. Campbell, and P. J. Tschaplinski: Climate change effects on watershed processes in British Columbia. In *Compendium of Forest Hydrology and Geomorphology in British Columbia*, Pike, R.G., T.E. Redding, R.D. Moore, R.D. Winker and K.D. Bladon (editors), B.C. Min. For. Range, For. Sci. Prog., Victoria, B.C. and FORREX Forum for Research and Extension in Natural Resources, Kamloops, B.C. Land Manag. Handb. 66. www.for.gov.bc.ca/hfd/pubs/Docs/Lmh/Lmh66.htm, 2010.

R Core Team: R: A Language and Environment for Statistical Computing, R Foundation for Statistical Computing, Vienna, Austria, available at: https://www.R-project.org/, last access: 18 October 2015.

Reager, J. T., Thomas, B. F., and Famiglietti, J. S.: River basin flood potential inferred using GRACE gravity observations at several months lead time. Nature Geoscience, 7, 588, 2014.

Rood, S.B., Samuelson, G.M, Weber, J.K., and Wywrot, K.A.: Twentieth-century decline in streamflows from the hydrographic apex of North America. J. Hydrol., 306, 215-233, doi: 10.1016/j.jhydrol.2004.09.010, 2005.

Rupp, D. E., Mote, P. W., Bindoff, N. L., Stott, P. A., and Robinson, D. A.: Detection and attribution of observed changes in Northern Hemisphere spring snow cover, J. Clim., 26, 6904-6914, 2013.

Salathé Jr, E. P., Hamlet, A. F., Mass, C. F., Lee, S. Y., Stumbaugh, M., and Steed, R.: Estimates of twenty-first-century flood risk in the Pacific Northwest based on regional climate model simulations, J. Hydrometeor., 15, 1881-1899, 2014.

Schnorbus, M. A., Bennett, K. E., and Werner, A. T.: Quantifying the water resources impacts of the mountain pine beetle and associated salvage harvest operations across a range of watershed scales: Hydrologic modelling of the Fraser River Basin, MBPI Project 7.29, Natural Resources Canada, Canadian Forest Service, Pacific Forestry Centre. Information Report BC-X-423, 64 pp., available via https://www.pacificclimate.org/resources/publications, 2010.

Schnorbus, M. A., Bennett, K. E., Werner, A. T., and Berland, A. J.: Hydrologic Impacts of Climate Change in the Peace, Campbell and Columbia Watersheds, British Columbia, Canada. PCIC Internal Report. Available via https://www.pacificclimate.org/resources/publications, 2011.

Septer, D.: Flooding and Landslide Events Southern British Columbia 1808-2006. *Victoria: BC Ministry of Environment*. Available as three separate files at: https://www.for.gov.bc.ca/hfd/library/documents/bib106111south1.pdf, https://www.for.gov.bc.ca/hfd/library/documents/bib106111south2.pdf, and https://www.for.gov.bc.ca/hfd/library/documents/bib106111south3.pdf, 2007.

Shabbar, A., Bonsal, B., and Khandekar, M.: Canadian Precipitation Patterns Associated with the Southern Oscillation. J. Climate, 10, 3016-3027, doi: 10.1175/1520-0442, 1997.

Shrestha, R. R., Schnorbus, M. A., Werner, A. T., and Berland, A. J.: Modelling spatial and temporal variability of hydrologic impacts of climate change in the Fraser River basin, British Columbia, Canada, Hydrol. Process., 26, 1840–1860. doi:10.1002/hyp.9283, 2012.

Shrestha, R. R., Peters, D. L. and Schnorbus, M. A.: Evaluating the ability of a hydrologic model to replicate hydro-ecologically relevant indicators, Hydrol. Process., 28, 4294–4310. doi:10.1002/hyp.9997, 2014.

Shumway, R. H. and Stoffer, D. S.: Time series analysis and its applications, with R examples, 3rd edition, Springer, New York, 2010.

Smakhtin, V.Y. and Masse, B.: Continuous daily hydrograph simulation using duration curves of a precipitation index, Hydrol. Process., 14, 1083–1100, 2000.

Surfleet, C.G. and Tullos, D.: Variability in effect of climate change on rain-on-snow peak flow events in a temperate climate, J. Hydrol., 479, 24-34, 2013.

Tan, X. and Gan, T. Y.: Nonstationary analysis of annual maximum streamflow of Canada, J. Climate, 28, 1788-1805, 2015.

Thorne, R. and Woo, M. K.: Streamflow response to climatic variability in a complex mountainous environment: Fraser River Basin, British Columbia, Canada, Hydrol. Process., 25, 3076-3085, 2011.

Wang, S. and Russell, H. A.: Forecasting snowmelt-induced flooding using GRACE satellite data: A case study for the Red River watershed, Can. J. Remote Sensing, 42, 203-213, 2016.

Water Survey of Canada: HYDAT Database, Natl. Water Data Arch. URL http://www.ec.gc.ca/rhc-wsc/default.asp?lang=En&n=9018B5EC-1/, last access 15 Sept., 2016.

Wever, N., Comola, F., Bavay, M., and Lehning, M.: Influence of snow surface processes on soil moisture dynamics and streamflow generation in alpine catchments, Hydrol. Earth Syst. Sci. Discuss., doi:10.5194/hess-2016-601, 2017.

Williams, C. J., McNamara, J. P., and Chandler, D. G.: Controls on the temporal and spatial variability of soil moisture in a mountainous landscape: The signature of snow and complex terrain, Hydrol. Earth Syst. Sci., 13, 1325–1336, doi:10.5194/hess-13-1325-2009, 2009.

Woo, M. and Thorne, R.: Comment on "Detection of Hydrologic Trends and Variability," by Burn, D.H. and Hag Elnur, M.A., 2002, Journal of Hydrology 255, 107–122, J. Hydrol., 277, 150-160, doi: 10.1016/S0022-1694(03)00079-9, 2003.

Tables

Table 1: Water Survey of Canada (WSC) hydrometric stations and corresponding basin and subbasin characteristics.

Station name (WSC ID)	Basin/subbasin name	Period of record	Subbasin Area [km^2]	Mean elevation [m]
Fraser R. at Hope (08MF005)	Fraser (FRB)	1912-2014	217000	1330
Fraser R. at Shelley (08KB001)	Upper Fraser	1951-2014	32400	1308
Quesnel R. near Quesnel (08KH006)	Quesnel	1939-2013	11500	1173
Thompson R. near Spences Bridge (08LF051)	Thompson-Nicola	1952-2013	54900	1747
Chilko R. near Redstone (08MA001)	Chilko	1927-2013	6940	1756

Table 2: Predictor variables and descriptions including their origin.

Predictor	Units	Description	Source
Maximum annual snow, SWE_{max} ; April 1 SWE, SWE_{Apr1}	mm	Annual maximum snow water equivalent (VIC); April 1 snow water equivalent (OBS)	VIC; MSS
October mean total column soil moisture	mm	Previous October mean value	VIC
Cold season rainfall	mm	Sum of rainfall between Oct 1 – Mar 31	PCIC-OBS
Spring rainfall	mm	Sum of rainfall between days of SWE_{max} (VIC) or SWE_{Apr1} (OBS) and annual maximum streamflow (APF)	PCIC-OBS
APF rainfall	mm	Sum of rainfall from 15 days prior to 5 days after APF	PCIC-OBS
Freezing degree days	°C	Absolute value of sum of negative daily mean $T < 0$ °C from Oct 1 – Mar 31	PCIC-OBS
Spring warming rate	°C day^{-1}	Slope of daily mean T between days of SWE_{max} and T_{max}	PCIC-OBS
Snowmelt rate	mm day^{-1}	Slope of daily SWE between dates of SWE_{max} and APF	VIC
Date of SWE_{max}, t_{SWEmax}	day	Julian day of maximum SWE	VIC
Melt season length, SWE_{len}	days	Date of 0.25 SWE_{max} minus date of SWE_{max}	VIC
NINO3.4 index	°C	HadISST1 anomaly over 5 °N -5 °S and 170 °W -120 °W	ESRL/GCOS
PDO index	°C	Leading PC of monthly SST anomalies in the North Pacific Ocean, poleward of 20 °N	JISAO

Table 3: Trends in observed and VIC-simulated variables over the period of each record. Results are only shown for those variables that contain a statistically significant trend at the $p < 0.05$ level. The trend was calculated using Sen's median slope estimator. Slightly different results are obtained for observed inputs to the VIC model due to the difference in start and end years of the time series. The residuals of each fit were checked for autocorrelation, with none detected in any fit.

Observations (1956-2006)			VIC Model (1955-2004)	
Variable (units of trend)	Trend (Sen)	Pearson R^2	Trend (Sen)	Pearson R^2
APDF (m^{-3} s^{-1} yr^{-1})	−36.5	0.10	–	–
Freezing degree days (°C day yr^{-1})	−6.29	0.14	−6.29	0.11
April-June mean T (°C day yr^{-1})	0.026	0.10	–	–
Spring Rain (mm yr^{-1})	–	–	0.927	0.13
PDO (yr^{-1})	0.035	0.16	0.038	0.17
Snowmelt rate (mm day^{-1} yr^{-1})	n/a	n/a	−0.0137	0.10
Melt season length (day yr^{-1})	n/a	n/a	0.225	0.12

Table 4: Fitted parameters from multilinear regression of the form: $Y = a_0 + a_1X_1 + a_2X_2 + a_3X_3 + \ldots$. For each fit, all partial p-values are less than 0.05. For each of the subbasins, only VIC-OBS results are given, due to the small number of April 1 observed SWE values available.

Basin / subbasin	Predictors				Coefficients					Partial F				F	R^2_{adj}
	X_1	X_2	X_3	X_4	a_0	a_1	a_2	a_3	a_4	F_1	F_2	F_3	F_4		
FRB															
OBS	SWE_{Apr1}	dT/dt	T_{amj}		4535	11.49	17068	−603.2		60.9	14.0	13.0		29.3	0.63
OBS$_{ext}$	SWE_{Apr1}	dT/dt	T_{amj}	NINO3.4	4106	10.48	17815	−494.3	−402.3	65.4	15.0	13.9	4.46	24.7	0.65
VIC-OBS	SWE_{max}	dT/dt	SWE_{len}	$d(SWE)/dt$	3239	37.14	26842	−57.69	1769.6	89.9	31.8			57.3	0.70
Upper Fraser	SWE_{max}	SWE_{len}	R_{Spring}		2413	5.257	−28.43	3.453		39.0	16.9	2.64		19.5	0.53
Quesnel	SWE_{max}	dT/dt	SM_{Sep}		−542.0	1.834	988.3	2291.2		55.1	19.0	5.77		26.6	0.61
Thompson-Nicola	SWE_{max}	dT/dt	$R_{Oct-Mar}$		−805.8	5.181	7199.8	4.341		97.4	39.1	7.75		48.1	0.75
Chilko	SWE_{max}	dT/dt			−142.6	1.152	786.2			56.5	8.45			32.5	0.56

Table 5: Top ten APF years at Fraser-Hope in the VIC-OBS simulation over the period 1955-2004, along with corresponding ranks of other basin-averaged predictors. Years in boldface font are highlighted in Fig. 9.

Rank APF	Year APF	Rank SWE$_{max}$	Rank SM	Rank FDD	Rank dT/dt	Rank Spring Rain
1	1982	6	6	14	1	47
2	**1972**	**2**	**1**	**4**	**21**	**26**
3	1974	1	4	17	39	22
4	**1958**	**25**	**13**	**46**	**5**	**49**
5	1956	10	7	1	11	50
6	2002	15	19	26	8	23
7	1967	7	9	28	7	39
8	**1999**	**4**	**8**	**44**	**45**	**1**
9	1997	5	2	9	22	13
10	1964	18	16	33	26	15
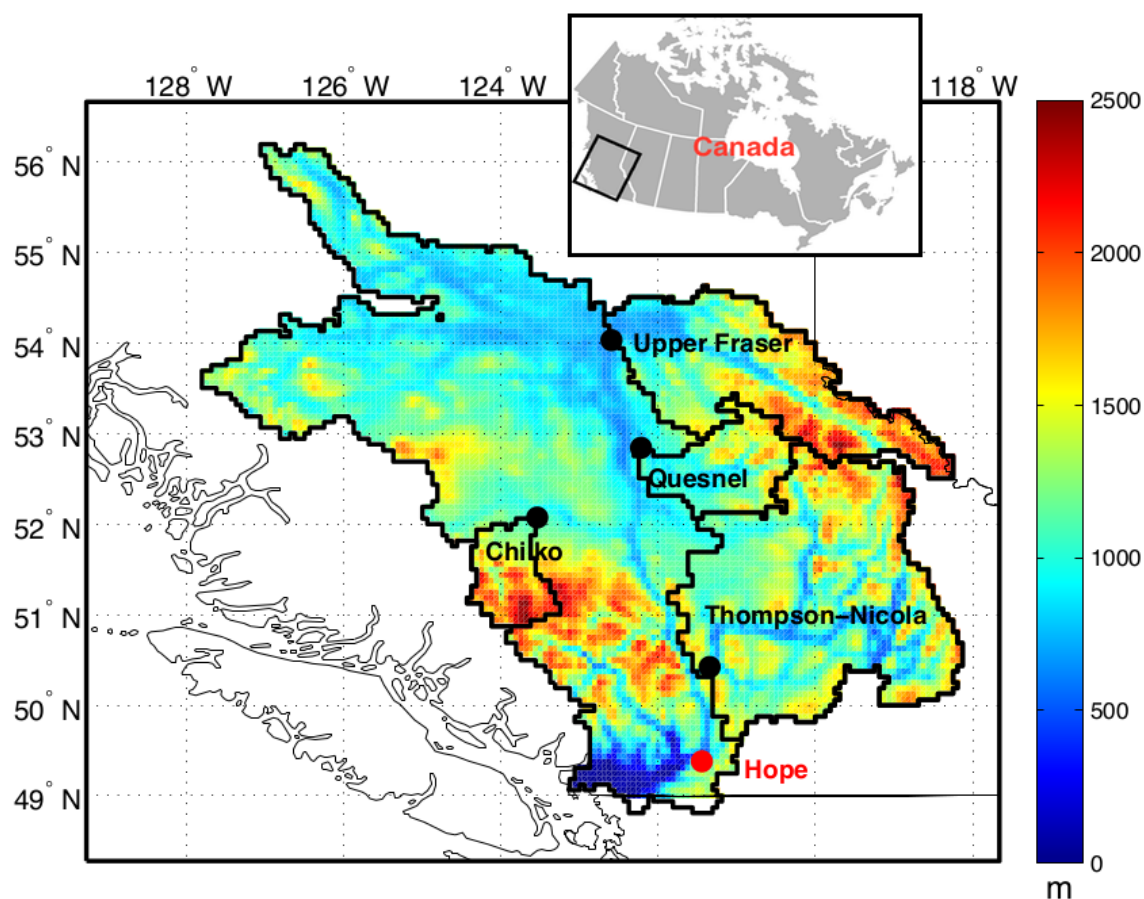
Figures

5   **Figure 1: The Fraser River Basin of British Columbia, Canada and four of its subbasins examined in this study. Colours correspond to elevations as used by the VIC model, at 1/16° horizontal resolution. Locations of streamflow gauge stations at the outlet to each subbasin are shown with black dots, while the major outlet for the FRB at Hope is shown with a red dot. Details of each subbasin are provided in Table 1.**
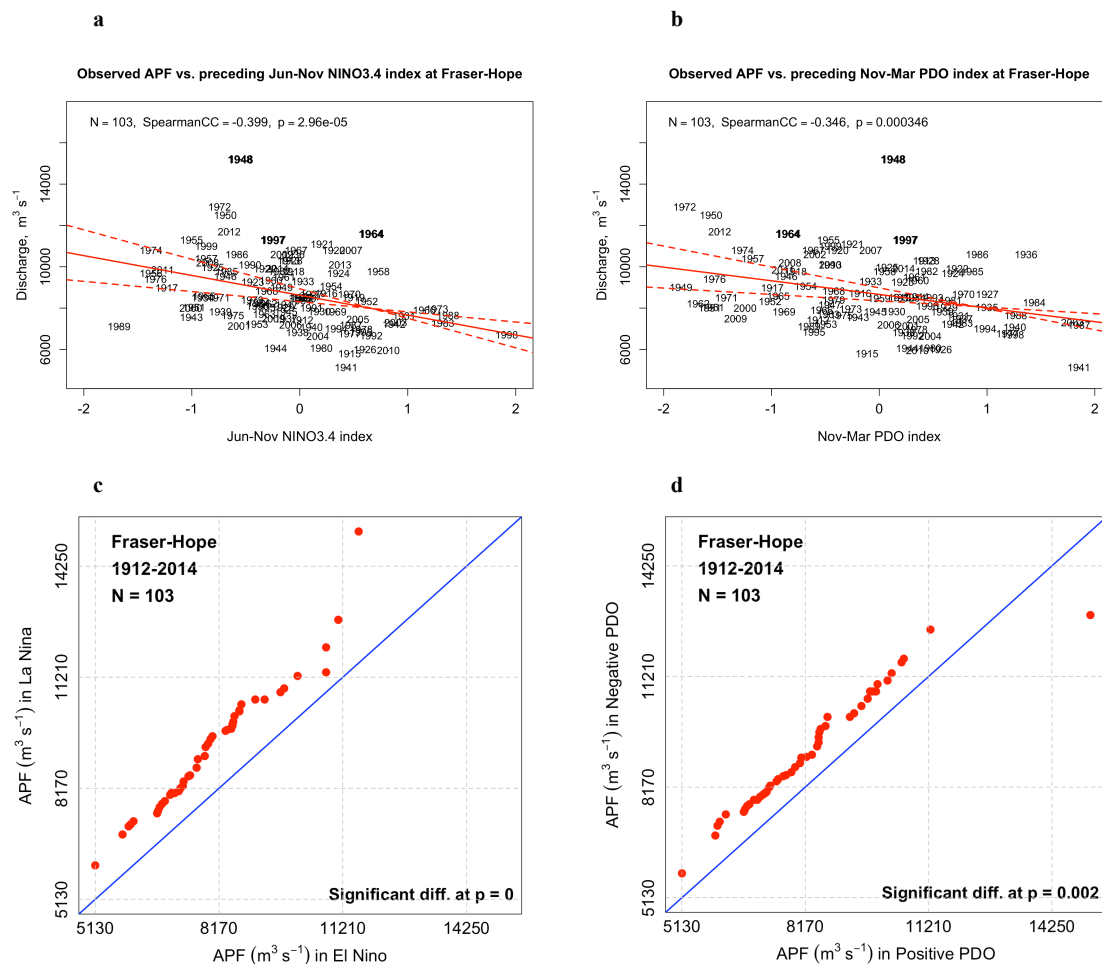
Figure 2: a) Regression of observed annual peak daily streamflow (APF) magnitude at Fraser-Hope hydrometric station (vertical axis) against the NINO3.4 index over the period 1912-2014. Year labels are plotted as individual points. b) Same as in a) but for the PDO index. Years in boldface font are discussed in the text of Sec. 3.2. c) Quantile-quantile plot of APF in years when the NINO3.4 index is in the negative (La Niña) phase (vertical axis) versus the positive (El Niño) phase (horizontal axis). The blue diagonal is the 1:1 line. Significance level using a permutation (resampling) test is shown at lower right. d) Same as in c) but for the PDO index.

a

b
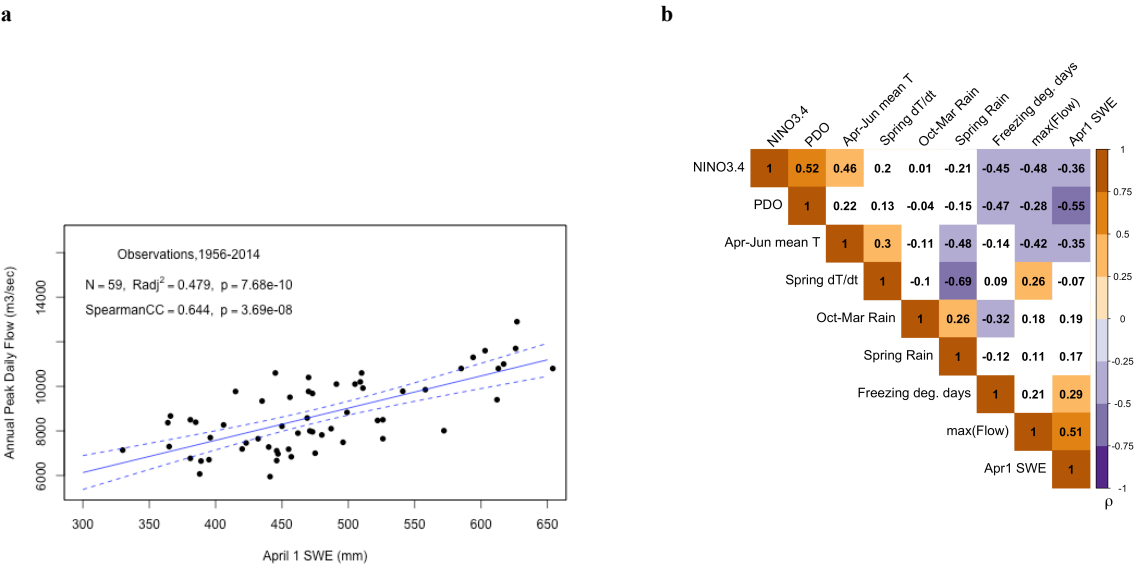
Figure 3: a) Regression of observed APF against basin-averaged April 1 SWE over the Fraser Basin, over the period of overlapping record, 1956-2014. The solid blue line is the least squares linear regression fit, while the dashed curves show the 95% confidence interval. Adjusted Pearson and Spearman rank correlation coefficients, along with their associated *p*-values, are indicated at upper left. b) Correlogram of all observed variables, averaged over the Fraser Basin over the common period of records, 1956-2006. Numerical values are Spearman rank correlation coefficients, and coloured squares indicate significant correlations at the *p* < 0.1 level.
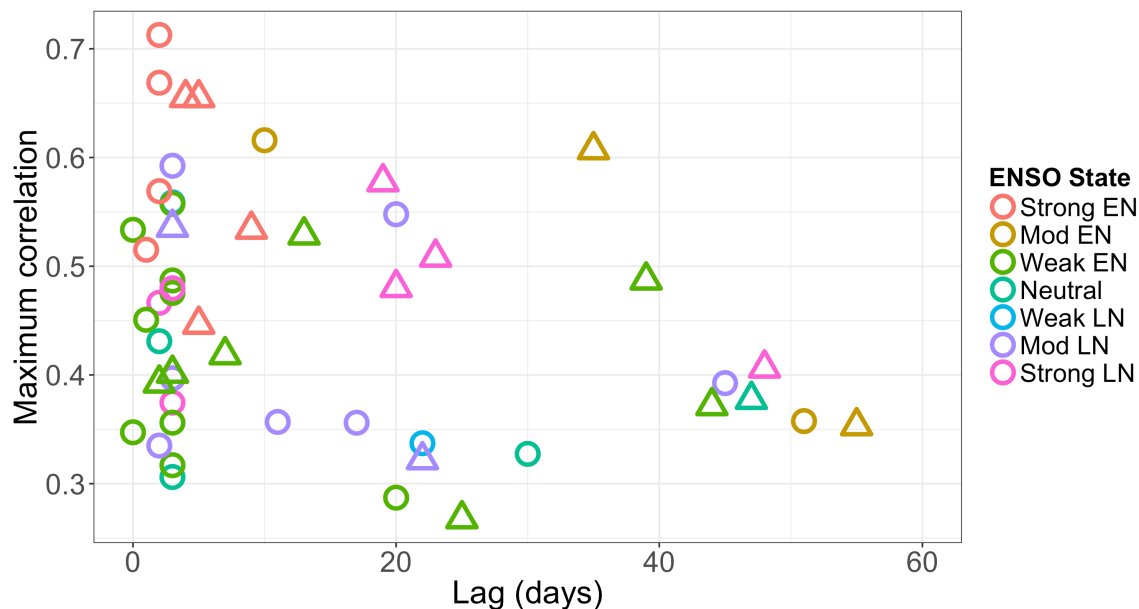
Figure 4: Results of lagged regression of FRB-averaged daily rainfall, characterized by the current rainfall index (CRI), on
5 **streamflow at Fraser-Hope. Only the subset of years wherein there exists a significant relationship between CRI and discharge are shown. The ENSO state, as specified in the legend according to colour, corresponds to the year preceding the rainfall and discharge, and was obtained from http://ggweather.com/enso/oni.htm, based on the same definition as used in the analysis of Sec. 3 (i.e. NINO3.4). The maximum correlation, max(ρ), is shown on the vertical axis, with the corresponding lag, τ, between rainfall and discharge on the horizontal axis. A positive lag means that streamflow lags CRI. *Circles*: Observed precipitation versus**
10 **observed discharge over the 1950-2006 period. *Triangles*: Observed precipitation versus VIC model-simulated discharge. All correlations are significant at the $p < 0.05$ level. Outlier points with lags > 60 days (with none exceeding max(ρ) = 0.42) are omitted from the plot.**
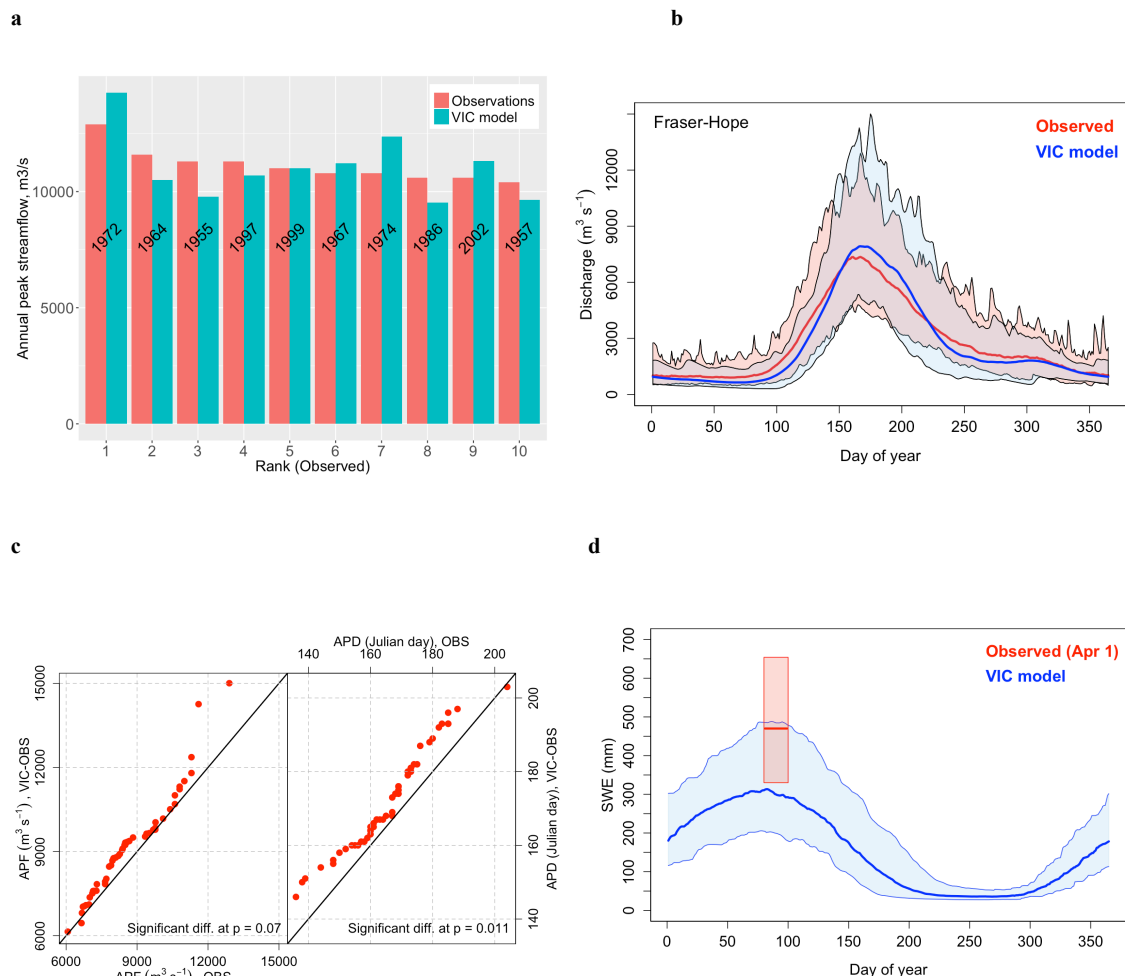
Figure 5: a) Annual peak daily streamflow (APF) magnitude in observations (red) and the VIC simulation (blue) at Fraser-Hope, ranked by observed values over 1955-2004. b) Annual cycle of daily streamflow in observations (red) and VIC simulation (blue). c) Quantile plots of VIC-simulated versus observed APF and APD. d) April 1 observed SWE (red) compared with annual cycle of SWE from VIC. Heavy curves show the multi-year median (1955-2004) while shaded areas show the interannual range.
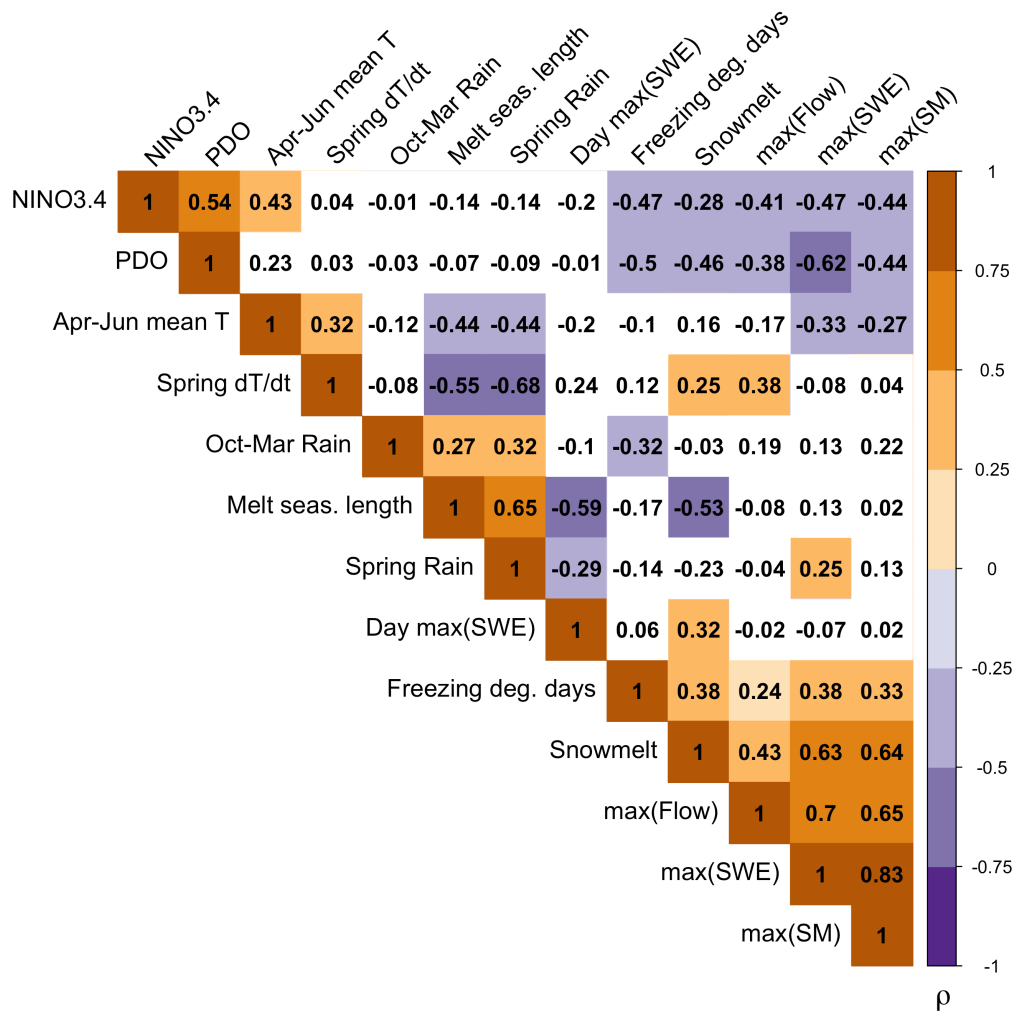
Figure 6: Correlogram of all observed and VIC-simulated variables, averaged over the Fraser Basin over the common period of records, 1955-2004. All values are Spearman rank correlation coefficients, and coloured squares indicate significant correlations at the $p < 0.1$ level. A hierarchical clustering algorithm has been applied to group like-with-like correlations.
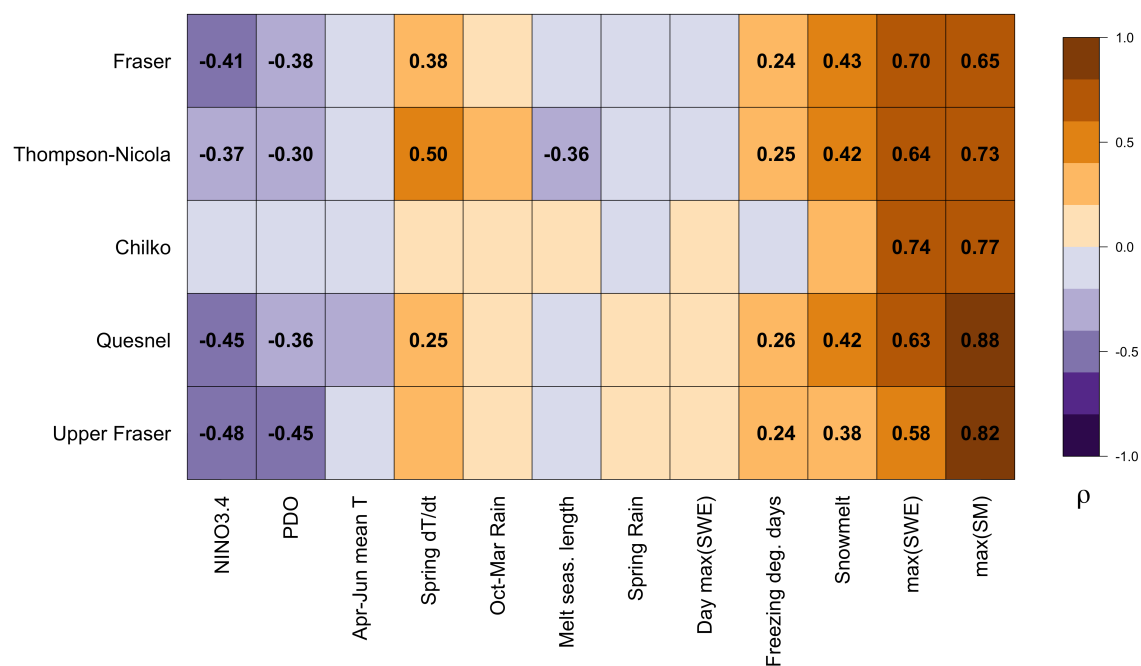
Figure 7: Correlogram of observed and VIC-simulated variables, averaged over each of the indicated subbasins over the 1955-2004 period, against APF at the subbasin outlet (Table 1). The cell values and colour scale indicate Spearman rank correlations, significant at the *p* < 0.10 level. The ordering of variable columns is the same as in Fig. 6, for ease of comparison.
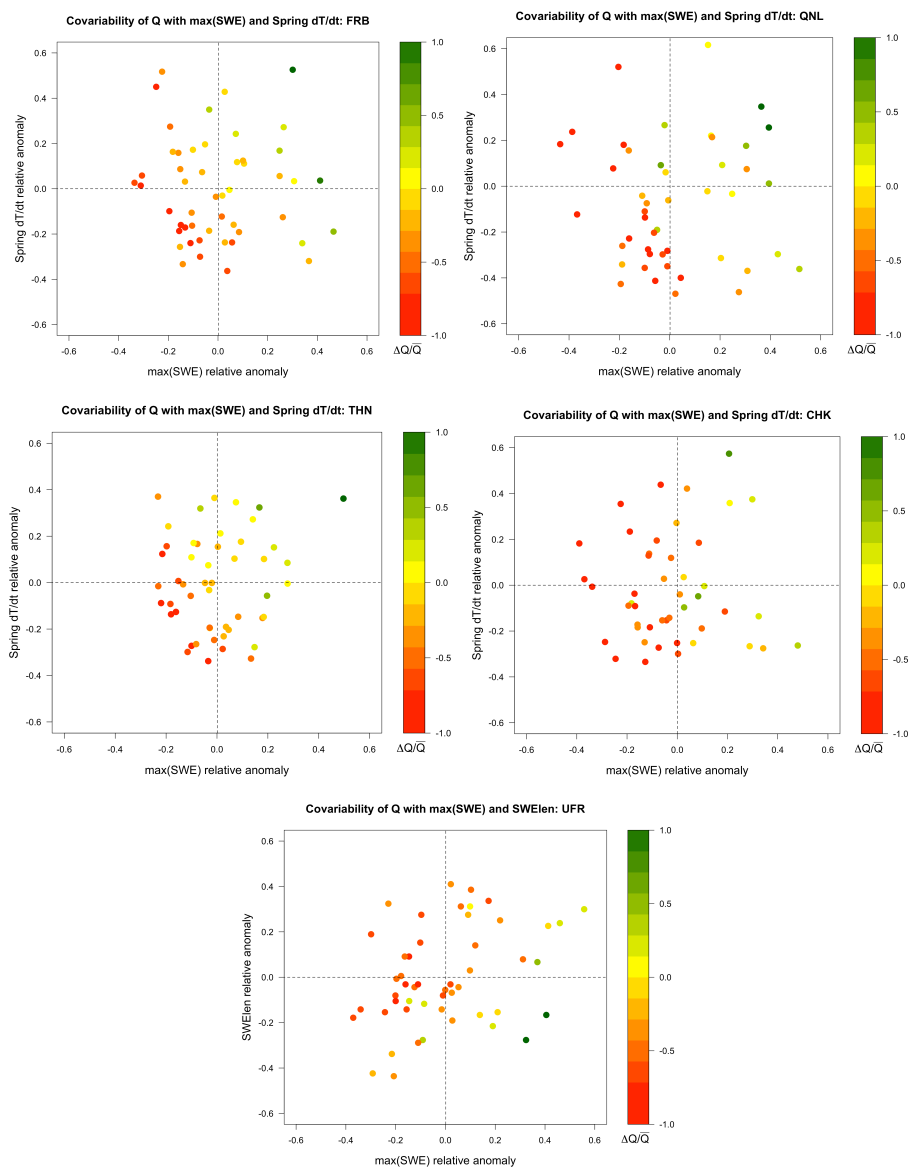
Figure 8: Scatterplots showing the co-dependence of relative APF, $\Delta Q / \overline{Q}$, (colour scale) on the two principal predictors from the MLR analysis (*x*- and *y*-axes), expressed as relative anomalies, in each basin. Counterclockwise from top left: entire Fraser (FRB), Thompson-Nicola (THN), Upper Fraser (UFR), Chilko (CHK) and Quesnel (QNL).
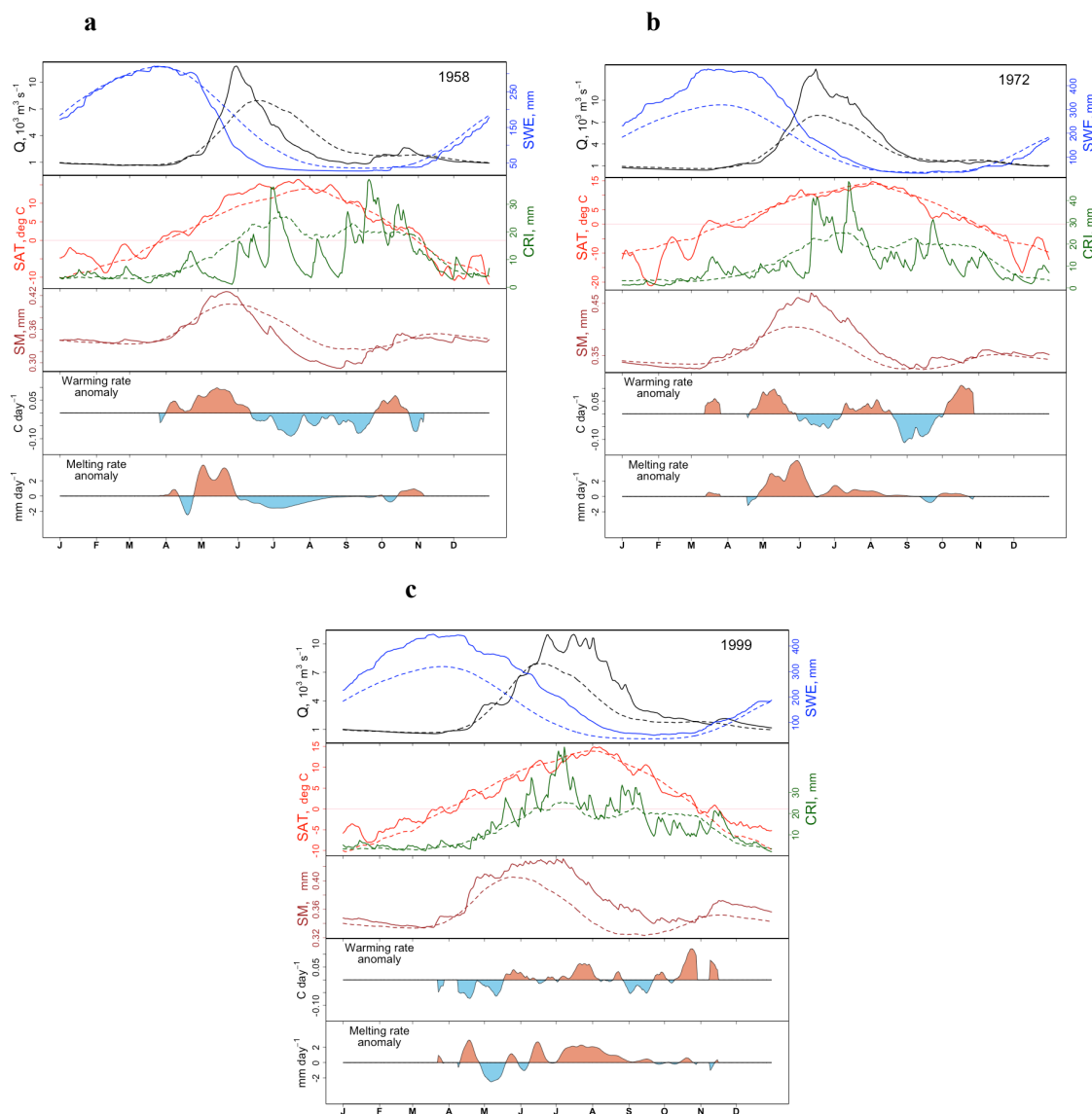
Figure 9: Annual cycles of key variables from the VIC simulation, constructed from daily output. Results for three high-APF years are shown: a) 1958; b) 1972; and c) 1999. In each panel, sub-panels show, from top to bottom: streamflow (black, left-hand axis); SWE (blue, right-hand axis); surface air temperature (red, left-hand axis); current rainfall index (green, right-hand axis); soil moisture (brown); warming rate anomaly; and melting rate anomaly. In the upper three sub-panels, solid curves show time series for the year indicated at top right, while dashed curves show the multi-year (1955-2004) mean climatology. The calculations underlying the lower two sub-panels are described in Sec. 4.